AGU PUBLICATIONS

Geochemistry, Geophysics, Geosystems

RESEARCH ARTICLE
10.1002/2014GC005691

Key Points:
- Most Afar faults divided into similar number of major and secondary segments
- In each hierarchical rank, the number of segments is between two to five
- Generic fault division makes deterministic heterogeneity in stress distribution

Supporting Information:
- Manighetti_et_al

Correspondence to:
I. Manighetti,
manighetti@geoazur.unice.fr

Citation:
Manighetti, I., C. Caulet, L. D. Barros, C. Perrin, F. Cappa, and Y. Gaudemer (2015), Generic along-strike segmentation of Afar normal faults, East Africa: Implications on fault growth and stress heterogeneity on seismogenic fault planes, *Geochem. Geophys. Geosyst.*, *16*, 443–467, doi:10.1002/2014GC005691.

Received 11 DEC 2014
Accepted 26 JAN 2015
Accepted article online 4 FEB 2015
Published online 18 FEB 2015

Generic along-strike segmentation of Afar normal faults, East Africa: Implications on fault growth and stress heterogeneity on seismogenic fault planes

I. Manighetti[1], C. Caulet[1], L. De Barros[1], C. Perrin[1], F. Cappa[1], and Y. Gaudemer[2]

[1]Université Nice Sophia-Antipolis, CNRS, IRD, Geoazur UMR 7329, Observatoire de la Côte d'Azur, Valbonne, France, [2]Institut de Physique du Globe de Paris, Paris, France

Abstract Understanding how natural faults are segmented along their length can provide useful insights into fault growth processes, stress distribution on fault planes, and earthquake dynamics. We use cumulative displacement profiles to analyze the two largest scales of segmentation of ~900 normal faults in Afar, East Africa. We build upon a prior study by Manighetti et al. (2009) and develop a new signal processing method aimed at recovering the number, position, displacement, and length of both the major (i.e., longest) and the subordinate, secondary segments within the faults. Regardless of their length, age, geographic location, total displacement, and slip rate, 90% of the faults contain two to five major segments, whereas more than 70% of these major segments are divided into two to four secondary segments. In each hierarchical rank of fault segmentation, most segments have a similar proportional length, whereas the number of segments slightly decreases with fault structural maturity. The along-strike segmentation of the Afar faults is thus generic at its two largest scales. We summarize published fault segment data on 42 normal, reverse, and strike-slip faults worldwide, and find a similar number (two to five) of major and secondary segments across the population. We suggest a fault growth scenario that might account for the generic large-scale segmentation of faults. The observation of a generic segmentation suggests that seismogenic fault planes are punctuated with a deterministic number of large stress concentrations, which are likely to control the initiation, arrest and hence extent and magnitude of earthquake ruptures.

1. Introduction

All faults (strike-slip, normal, and reverse) are segmented along their strike; that is, although they appear overall as planar continuous structures, faults are in fact divided into a number of distinct subparallel sections or "segments" separated by geometrical discontinuities referred to as "intersegments" (Figure 1) [e.g., *Tchalenko and Berberian*, 1975; *Segall and Pollard*, 1980; *Sibson*, 1986; *Barka and Kandisky-Cade*, 1988; *Aydin and Schultz*, 1990; *Scholz*, 1991; *Peacock*, 1991; *Ferrill et al*., 1999; *Zhang et al*., 1999; *Walsh et al*., 2003; *Ben-Zion and Sammis*, 2003; *Soliva and Benedicto*, 2004; *de Joussineau and Aydin*, 2009; *Giba et al*., 2012]. Fault segments may have various lengths. When a fault is young and immature, its segments are hardly connected [e.g., *Walsh and Watterson*, 1991; *Trudgill and Cartwright*, 1994; *Mansfield and Cartwright*, 2001], and these soft connections make the fault fairly discontinuous (Figure 1a). Conversely, when a fault has long been established, its segments are commonly strongly connected to each other [e.g., *Walsh and Watterson*, 1991; *Trudgill and Cartwright*, 1994; *Manighetti et al*., 2007, 2009], making the fault a more continuous feature (Figure 1a).

Here we question whether the along-strike segmentation of natural faults has scale properties, and whether segmentation is case-dependent or generic. Addressing these questions is important. First, the segmentation of faults is likely an outcome of the fault growth process, and therefore, understanding the way natural faults are segmented may provide useful insights into fault mechanics. At present, our understanding of fault mechanics relies on theoretical models, most are based on simple linear elastic fracture mechanics or elastic-plastic theories ["crack models," e.g., *Griffith*, 1920, 1924; *Eshelby*, 1957; *Dugdale*, 1960; *Nabarro*, 1967; *Kanninen and Popelar*, 1985; *Pollard and Segall*, 1987 for seminal papers; and e.g., *Leblond et al*., 2011; *Johri et al*., 2014, for more recent developments or discussion]. Yet an increasing number of observations on natural faults suggest that these models do not fully reproduce the fault properties and behaviors (see

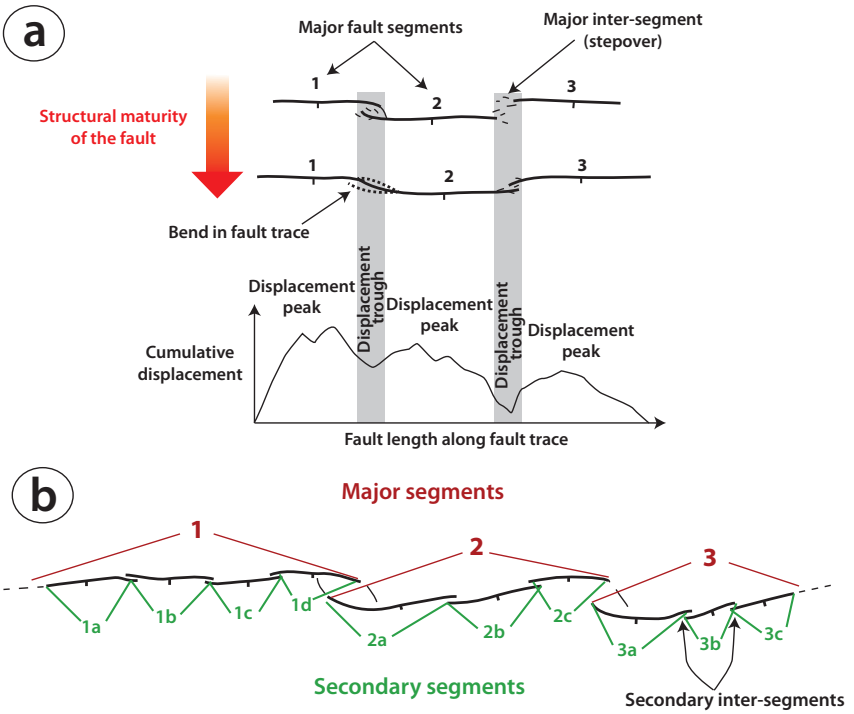

Figure 1. Schematic representation of the two largest scales of fault segmentation analyzed in this study. In both figures, the fault is the entire black trace. (a) Major fault segments as commonly seen in Figure 1(top plots) surface fault trace geometry and in Figure 1(bottom plots) fault cumulative displacement profile. Major segments are those with a length of the same order than that of the fault they belong to. Three major segments are shown, which become connected as fault maturity increases. The major segments form large displacement peaks in the fault displacement profile, whereas the intersegment zones that separate them (commonly step-overs or bends, sites of multiple cracking) coincide with narrow displacement troughs. (b) Each major segment is itself divided into a number of subordinate, secondary segments (secondary segments thus have a length of the same order than that of the major segment they belong to), separated by secondary intersegments.

discussion in *Manighetti et al*. [2001a, 2004, 2005], *Davis et al*. [2005], and *Cappa et al*. [2014]). Therefore, acquiring more empirical data on natural faults is needed to further constrain the theoretical models. Second, independent of their slip mode, earthquakes are sensitive to fault segmentation. Most earthquakes do not rupture the entire length of a fault on which they nucleate, but only one or a few of its segments [e.g., *Schwartz and Coppersmith*, 1984; *DePolo et al*., 1991; *Machette et al*., 1991; *Zhang et al*., 1991, 1999; *Harkins et al*., 2005; *Bull et al*., 2006; *Hecker et al*., 2010], sometimes in a cascade-like fashion across the intersegment zones [e.g., *Manighetti et al*., 2007; *Shaw and Dieterich*, 2007; *Kase*, 2010; *Schlagenhauf et al*., 2011; *Benedetti et al*., 2013]. Furthermore, many earthquake ruptures have been observed to terminate at a fault intersegment [*Schwartz and Coppersmith*, 1984; *Sibson*, 1985, 1986; *King and Nabelek*, 1985; *Barka and Kadinsky-Cade*, 1988; *Knuepfer*, 1989; *Zhang et al*., 1999; *Lettis et al*., 2002; *Das*, 2003; *Manighetti et al*., 2005; *Wesnousky*, 2006; *Black and Jackson*, 2008]. Therefore, the along-strike segmentation of faults is a controlling factor of the earthquake process. This is especially true for the largest scales of fault segmentation that is the longest segments within faults, because those are the most prone to divide the fault plane across the seismogenic crust [e.g., *Sibson*, 1986]. Fault segmentation also dictates the magnitude of an earthquake because magnitude depends on the rupture length, which itself depends on the number of ruptured segments along a fault [e.g., *Manighetti et al*., 2007; *Oglesby*, 2008; *Kase*, 2010].

A critical issue is that the scales and properties of fault segmentation are still poorly known. While studies have been conducted to describe the along-strike segmentation of a single fault (e.g., references in Table 1 described further below), very few works have analyzed large fault populations to examine the possible common and/or distinct segmentation properties. Furthermore, these works suggest different results. Based on statistical analyses of lineaments along strike-slip faults, laboratory experiments, seismological inferences, and roughness of exposed fault planes, some studies argue that fault segmentation is fractal [e.g., *Scholz and Aviles*, 1986; *Okubo and Aki*, 1987; *Power and Tullis*, 1991; *Sammis et al*., 1999; *Seno*, 2003; *Renard*

et al., 2006; *Candela et al*., 2009; *Andrews and Barral*, 2011]. Based on the analysis of ~900 normal faults, *Manighetti et al*. [2009] suggest that the number of longest segments within faults is similar among the faults, and therefore that the length of these segments is variable from one fault to another. In opposition with this result, *Klinger* [2010] and *Klinger et al*. [2005, 2013] suggest, based on the analysis of a few large earthquake ruptures, that strike-slip faults are divided into a variable number of segments of similar length, about 20 km.

Several major questions thus remain: What are the different scales of fault segmentation? Is fault segmentation fractal? Do fault segments at various scales exhibit common or variable properties? Are faults rather divided into constant number-segments or constant length-segments? Does the tectonic setting or type of fault play a role on the observed fault segmentation patterns?

The along-strike segmentation of faults can be observed in the surface fault trace geometry (Figures 1 and 2; references in Table 1), as in the fault cumulative displacement profiles (Figures 1a and 2c), which depict the distribution of the total displacement accumulated along a fault over its whole history. The intersegment zones that separate the fault segments, especially the longest segments, are zones of cumulative displacement deficit (Figures 1 and 2) [e.g., *Dawers and Anders*, 1995; *Mansfield and Cartwright*, 1996, 2001; *Davis et al*., 2005; *Bull et al*., 2006]. Therefore, they appear as narrow troughs in fault cumulative displacement profiles, separating large peaks that represent the displacement on the fault segments (Figures 1 and 2) [e.g., *Ellis and Dunlap*, 1988; *Peacock and Sanderson*, 1991; *Peacock*, 1991; *Willemse*, 1997; *Mansfield and Cartwright*, 2001; *Manighetti et al*., 2001a, 2001b; *Walsh et al*., 2003; *Soliva and Benedicto*, 2004; *Davis et al*., 2005]. Fault traces and cumulative displacement profiles do not always portray the full range of scales of the fault segmentation however, because the complexities of the fault traces and of the displacement profiles are smoothed out as the fault accumulates more displacement and becomes more mature [e.g., *Wesnousky*, 1988; *Stirling et al*., 1996; *Sagy et al*., 2007; *de Joussineau and Aydin*, 2009]. Therefore, it seems difficult to analyze the full range of scales in fault segmentation with other means than experimental works [e.g., *Clifton et al*., 2000; *Otsuki and Dilov*, 2005; *Schlagenhauf et al*., 2008].

We thus address the questions above by analyzing the relatively longest segments in a dense fault population. More specifically, we analyze the cumulative displacement profiles for ~900 normal active faults in the Afar region, East Africa Rift zone (Figure 2a), which span a broad range of lengths (1–10^2 km) and cumulative displacements (1–10^3 m) [e.g., *Manighetti et al*., 1997, 1998, 2001a, 2001b]. The faults are younger than ~1 Ma, and hence relatively immature. Using two signal processing methods (Fourier and S-transform), *Manighetti et al*. [2009] analyzed the cumulative displacement profiles of these ~900 faults. Their aim was to recover the number of longest segments within the faults. They found that, independent of the fault length, total displacement, initiation age, geographic location, proximity to other faults, and slip rate, most faults have a similar number of longest segments, in the range of two to five. Their study, however, did not provide information on the position and size (i.e., length and total displacement) of the major fault segments, and did not examine the subordinate segmentation of these longest segments. Here we build upon this prior work to provide this new information. We develop a novel signal processing method (low-pass filtering), which we apply to the ~900 fault displacement profiles to quantify the position, displacement, and length of the longest segments within each of the ~900 faults (these longest segments are referred to as "major" or "first-order" segments, Figure 1b). We then similarly analyze the displacement distribution on each of the ~2900 identified major segments to recover the number, position, displacement and length of the subordinate, "secondary" (or "second-order") segments within the major segments (Figure 1b).

We find that the along-strike segmentation of Afar normal faults obeys generic and similar properties at both the largest scale (major segments) and the subordinate scale (secondary segments). We define several scaling relations for characterization of fault segmentation properties. These deterministic properties shed light on fault growth processes and have implications for the static stress heterogeneity on seismogenic fault planes.

2. Data Sets

The ~900 normal faults are located in the desert Afar region, East Africa rift zone, 95% on land and 5% in shallow water (Figures 2a and 2b). The faults were mapped and their cumulative displacement profiles measured in prior studies (Figure 2b) [*Manighetti et al*., 1997, 1998, 2001a, 2001b, 2009; *Audin et al*., 2001]. Each fault is defined by a continuous surface trace. All form steep (≥~70°) escarpments in the topography

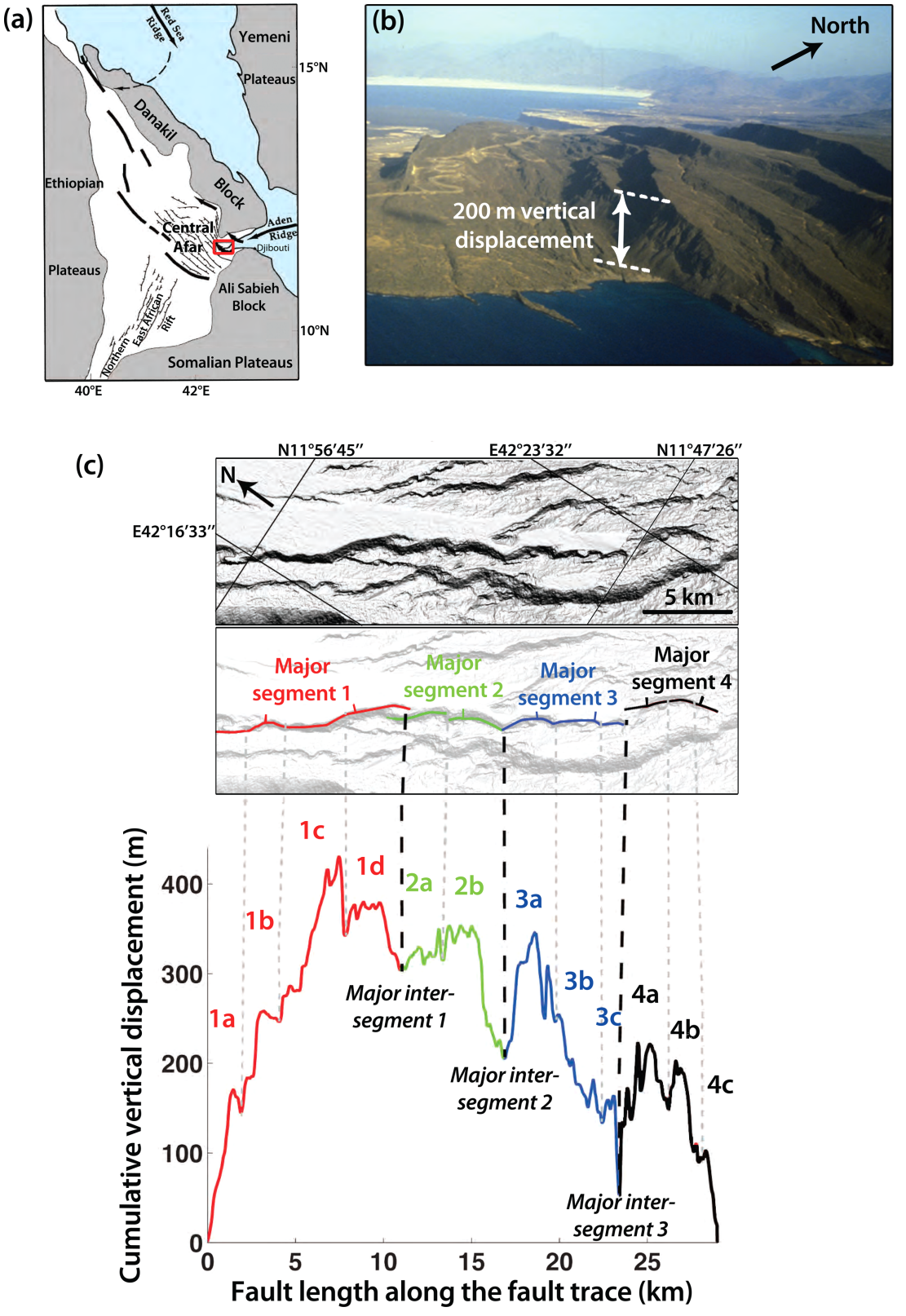

and bathymetry (Figure 2b), which have been shown to provide well-preserved records of the total vertical displacement accumulated on the faults over their whole history [*Manighetti et al*., 1997, 1998, 2001a, 2001b, 2009; *Audin et al*., 2001]. Fourteen percent of the faults are located in the Asal-Ghoubbet rift [80 faults in the on land "Asal" part of the rift, and 47 in its underwater "Ghoubbet" section, e.g., *Manighetti et al*., 1998, 2001a], while the remaining 86% of the faults are located in the Afar region outside of the numerous rift segments (Figure 2a) [*Manighetti et al*., 2001b].

The cumulative displacement profiles were extracted from three digital elevation models (DEMs). All profiles were derived from a large number of measurements, on average 10 per hundred meters of fault length. In Asal-Ghoubbet, two different DEMs cover the Asal and the Ghoubbet regions, both have a pixel size of ~15 m, an absolute vertical height accuracy of ~3 m, and a relative vertical height accuracy of ~1 m [e.g., *De Chabalier and Avouac*, 1994; *Audin et al*., 2001 where the two DEM sources can be found]. In the Afar region, the data were extracted from the worldwide SRTM3 DEM which has a pixel size of ~90 m, an absolute vertical height accuracy <16 m, and a relative vertical height accuracy <10 m [e.g., *Farr and Kobrick*, 2000; *Werner*, 2001; *Rabus et al*., 2003]. However, *Gorokhovich and Voustianiouk* [2006] have shown that, even in regions with vegetation, the vertical precision of the SRTM3 DEM is actually better, with an absolute vertical height accuracy in the range of 4–8 m, and a relative vertical height accuracy about half the absolute error (~4 m). In Afar, where vegetation and buildings are lacking, the ~4 m uncertainty between relative elevations is thus likely to apply.

To ensure that the displacement profiles are well resolved, *Manighetti et al*. [2009] limited the data set to faults with maximum displacement >60 m for Afar faults and >3 m for Asal-Ghoubbet faults. The faults span a broad range of lengths (0.3–65 km, fault length referred to as L in the following, Figure 3a) and maximum cumulative displacements (3–1300 m, maximum displacement referred to as D_{max} in the following; Figure 3b and supporting information Figure S1 for faults discriminated from their location and hence from their DEM source). Their maximum displacement and length values are consistent with the linear scaling commonly observed for faults worldwide ($D_{max} \sim 10^{-2} * L$, Figure 3c) [e.g., *Cowie and Scholz*, 1992; *Dawers et al*., 1993; *Schlische et al*., 1996; *Scholz*, 2002]. The lengths of the faults vary from much smaller (53% of fault lengths are $<W_{seism}$, where W_{seism} is the thickness of seismogenic crust) to much larger (47% of fault lengths are up to ~6 * W_{seism}) than the thickness of the crust which they cut (W_{seism}, ~5 km in Asal-Ghoubbet and ~10 km elsewhere) [e.g., *Manighetti et al*., 2001b; *Doubre et al*., 2007a, 2007b] (Figure 3d and supporting information Figure S1). The age of fault initiation varies between ~10^4 and 10^6 year, while the fault slip rates range between ~0.5 and ~5 mm/yr [e.g., *Stein et al*., 1991; *Manighetti et al*., 1998, 2001a, 2001b].

3. Data Processing

We highlight six examples of displacement profiles measured on Afar and Asal-Ghoubbet faults with different location, length, and maximum cumulative displacement (Figure 4). Most profiles have a fairly triangular and asymmetric envelope shape, consistent with the generic shape of displacement-length distribution observed on both long-term faults [e.g., *Manighetti et al*., 2001a, 2001b, 2009; *Scholz*, 2002; *Soliva and Benedicto*, 2004; *Nicol et al*., 2005; *Martel and Shacat*, 2006 for normal faults; e.g., *Peacock*, 1991; *Bürgmann et al*., 1994; *McGrath and Davison*, 1995; *Pachell and Evans*, 2002; *Farbod et al*., 2011 for strike-slip faults; e.g., *Ellis and Dunlap*, 1988; *Shaw et al*., 2002; *Davis et al*., 2005 for reverse faults] and individual earthquake ruptures [e.g., *Scholz and*

Figure 2. Tectonic setting of analyzed faults and description of major and secondary segments in one Afar fault case. (a) Simplified fault map of Afar (modified from *Manighetti et al*. [2001b]). Seawater is in blue, area of rift-related extension in white, unextended continental crust in gray, propagating rifts and ridges in thick black lines and arrows, principal normal faults in thin black lines with hachure ticks. The "Afar" fault set is located in "Central Afar" (i.e., white area) whereas the "Asal-Ghoubbet" fault set is located in the red-squared area [see *Manighetti et al*., 1997, 1998, 2001, for more details]. (b) Field view of active normal fault escarpments in Asal-Ghoubbet rift. Most fault scarps are steep (dip ≥ ~70°) and they vertically offset the planar upper flow surfaces of homogeneous basaltic lavas (here dated at ~30 ka; see references above). An example of the measured vertical cumulative displacement is indicated on the foreground fault scarp. (c) Identification of major (e.g., 1, 2, 3, 4) and secondary segments (e.g., a, b, c, etc.) in (top) both the surface fault trace and (bottom) the fault cumulative displacement profile. The fault trace is shown on SRTM3 topography illuminated from the west. The cumulative displacement is measured along the surface fault trace. The major segments, discriminated with colors, appear as distinct collinear sections in the fault trace, separated by bends or step-overs. In the displacement profile, they appear as large displacement peaks separated by narrow zones of cumulative displacement deficit (major intersegments). The secondary segments (numbered 1a, 1b etc.) also appear as distinguishable subsections in the fault trace separated by bends in fault strike. In the displacement profile, they appear as narrow displacement peaks separated by narrow and small zones of cumulative displacement deficit (secondary intersegments).

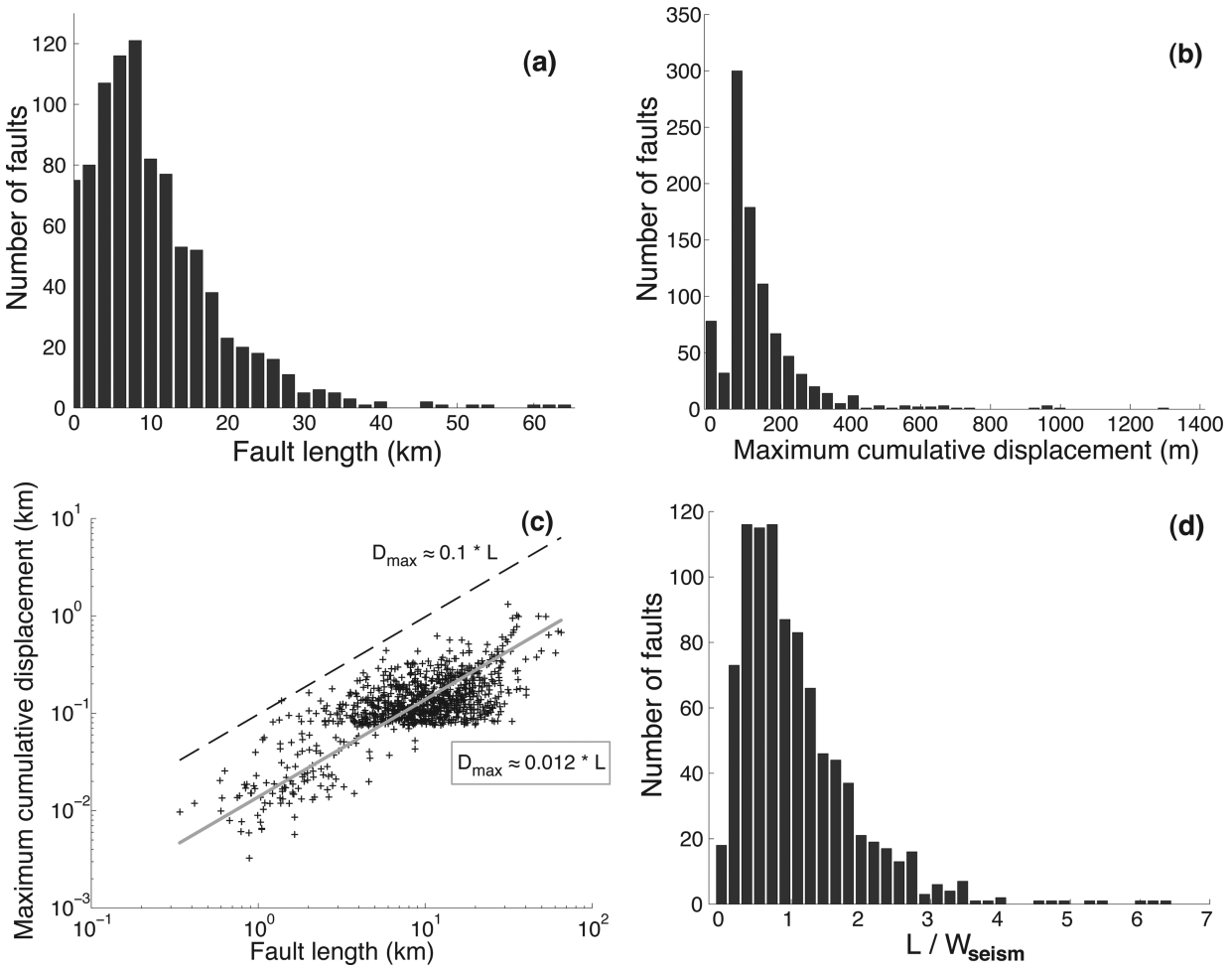

Figure 3. Distribution of lengths and maximum cumulative displacements for the entire fault population (~900 faults). The fault population is the same population as that previously described in *Manighetti et al*. [2009]. We have however excluded ~20 short displacement-length profiles with too few data points. (a) Length distribution; (b) maximum cumulative displacement distribution; (c) maximum cumulative displacement to length scaling. The gray line is the linear regression fit to the data (Dmax ~0.012 L, linear correlation coefficient R = 0.62). A power law Dmax ~0.03 * L0.7 fits the data equally well (linear correlation coefficient between log(xi) and log(yi) R = 0.61). The dotted line indicates the threshold Dmax/L ~0.1 value beyond which no fault displacement-length data exists; (d) distribution of fault lengths relative to seismogenic crust thickness (Wseism). See Figure 1 in supporting information for a similar figure with faults discriminated by location.

Lawler, 2004; *Manighetti et al*., 2005; *Wesnousky*, 2008; *Perrin et al*., 2012; *Cappa et al*., 2014]. On each fault, the distribution of cumulative displacement along-strike appears as a fluctuating signal, dominated by large peaks separated by narrower troughs (Figure 4a). As shown in *Manighetti et al*. [2009], the wider peaks of high displacement coincide with the major segments of the faults (as defined in Figures 1 and 2), whereas the troughs are the zones of displacement deficit that separate the major segments (intersegments). The same observation can be made when looking at major segments individually: major segment profiles include wide peaks separated by narrow troughs (Figures 2 and 4). The largest of these peaks coincide with the secondary segments along the fault (Figures 1 and 2), as shown in the example in Figure 2c.

Before processing the displacement profiles, we normalized the profile lengths (supporting information Figure S2b). Such normalization is needed to perform a length-independent analysis. We also examined whether the displacement distributions show the generic triangular shape. This question is important to examine the possible relations between overall displacement distribution and fault segmentation. We determined, through a least square calculation, whether each displacement profile is best adjusted by a triangular or by an elliptical function (Figure 4a; the elliptical function is that predicted from the elastic crack theory, see discussion in *Manighetti et al*. [2001a, 2001b] and *Scholz* [2002]). We confirm that ~70% of the faults have an asymmetric triangular displacement profile (supporting information Figure S4). The degree of asymmetry varies however across the fault population (supporting information Figure S4).

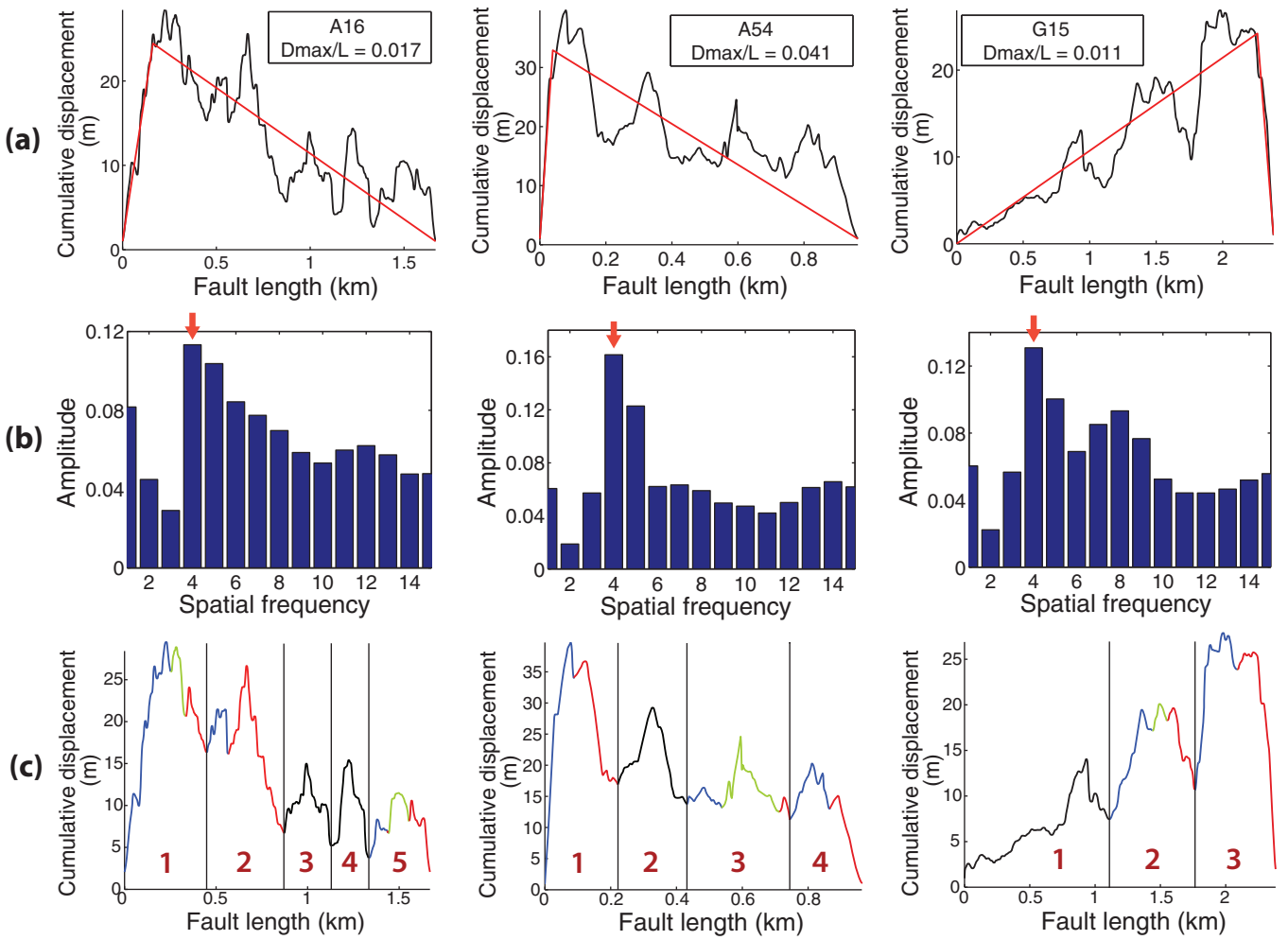

Figure 4. Segment identification on six example fault displacement profiles. (a) Measured cumulative displacement profiles (in black) along the faults whose name is indicated in the square (A for Asal, G for Ghoubbet, S for "stratoid", i.e., Afar). The fault length is the length measured along the fault trace. The maximum displacement to length ratio of the faults is indicated. The best fitting function (triangular or elliptical) is in red. (b) Histograms of the S-transform amplitude at the different spatial frequencies, for each displacement profile above. The S-transform has been applied to the normalized displacement profiles. The plots are made for spatial frequencies in the range 0–15, but we have verified that the results are unchanged for larger ranges. In most examples, the greatest signal energy (largest amplitude indicated with a red arrow) occurs over a narrow range of spatial frequencies, between two and five. Most example profiles also contain higher frequencies hence shorter lengths of displacement oscillations. (c) Identification of the major and secondary segments along each fault above, performed with the low-pass filtering method. The profiles are shown with their actual length, but the processing was done on normalized profiles. Vertical lines separate the recognized major segments, here numbered from left to right. Colors discriminate the secondary segments within each major segment.

We then processed the cumulative displacement profiles using two different methods. We first analyzed the fault profiles using the S-transform method described in *Manighetti et al.* [2009]. The S-transform approach is a space-frequency representation of a fluctuating signal that is based on a wavelet-type analysis through a Gaussian window whose width scales inversely with the spatial frequency [*Stockwell et al.*, 1996]. The S-transform can thus be used to characterize local spectral properties such as dominant spatial frequencies in the displacement distributions. As the profile lengths are normalized, dominant spatial frequencies correspond to dominant displacement oscillations, which coincide with fault segments [*Manighetti et al.*, 2009]. Our objective is not to duplicate the previous work. Yet to develop another signal processing approach best appropriate to recover the location and size of the fault segments, as we do below, we need to have a prior approximate knowledge of the possible number of fault segments (to define the cutoff frequency, see below). The S-transform approach fulfills this need and therefore we use it as a first step.

In contrast to *Manighetti et al.* [2009], we have applied the S-transform method to the actual displacement profiles, not to profiles from which the average envelope triangular or elliptical shape has been subtracted. For each of the ~900 fault displacement profiles, we have built the histogram of the maximum amplitude

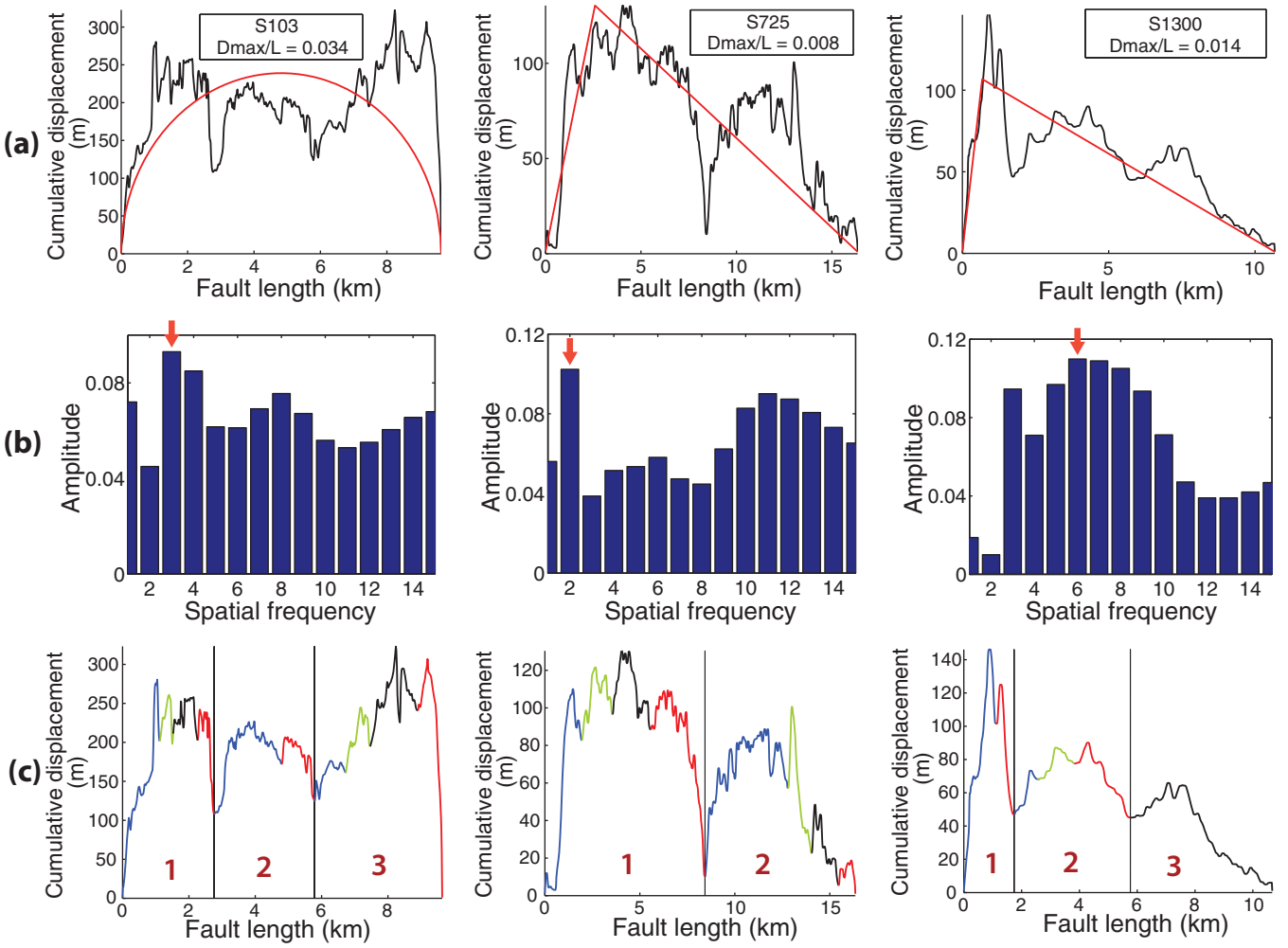

Figure 4. (Continued)

at each spatial frequency (supporting information Figure S2c and examples in Figure 4b). From each histogram, we have recorded the spatial frequency at which the S-transform amplitude is the highest (indicated with a red arrow in Figure 4b). This spatial frequency indicates the number of major segments in the corresponding fault [e.g., *Manighetti et al.*, 2009]. However, an underlying assumption is that all major segments within a fault have a similar length. This is not necessarily the case, leading to a high amplitude across a few consecutive spatial frequencies (see examples A16, S103, and S1300 in Figure 4b). We have built a cumulative histogram of the number of major segments for the entire fault population (Figure 5). This histogram, which we describe in further detail in section 4, confirms, as shown by *Manighetti et al.* [2009], that the majority of faults are divided into a similar number of major segments, in the range of two to five. This narrow range of values serves as a basis to define the cutoff frequency in the second approach that we describe now.

We have processed the fault displacement profiles with another, low-pass filtering method (supporting information Figure S2d). The filtering [Butterworth function; *Butterworth*, 1930] is aimed at removing the high-frequency components of the displacement fluctuations so as to emphasize the widest displacement oscillations. The cutoff frequency of the filter (i.e., the spatial frequency above which the frequencies are eliminated) is a crucial parameter. We have tested different cutoff frequencies (F_c) slightly higher than the number of major segments revealed by the S-transform approach, and we found that F_c values in the range of five to seven best emphasize the widest displacement peaks, in agreement with the visual observation of the profiles. We have thus applied a cutoff frequency of six to all fault displacement profiles except those for which the maximum S-transform amplitude was found at a very low spatial frequency (one or two). For these latter

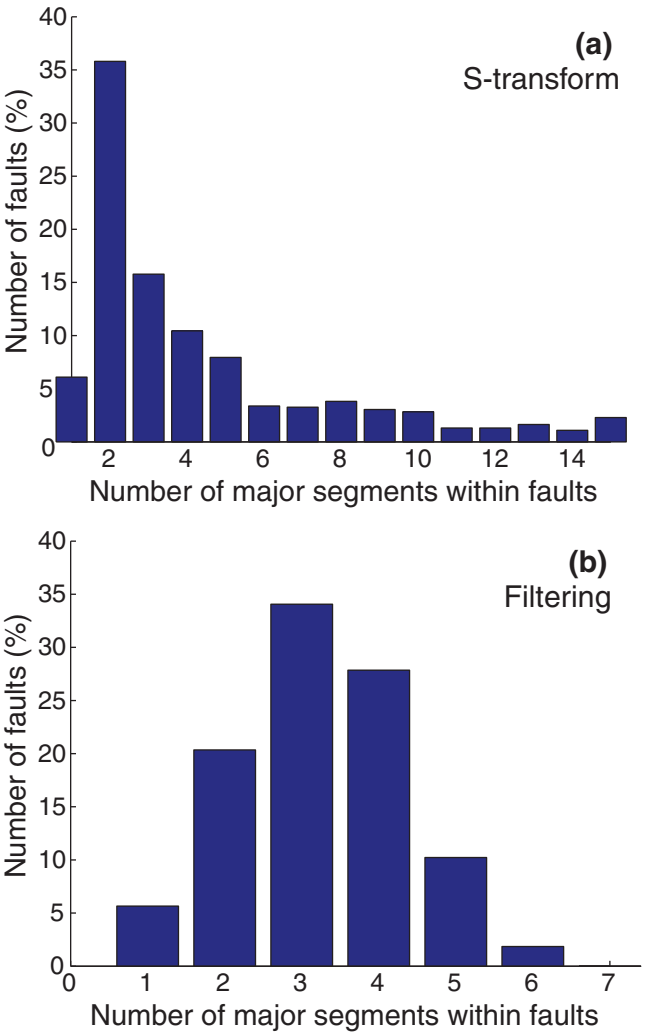

Figure 5. Distribution of the number of major segments within faults for the entire fault population. (a) determined from S-transform method; (b) determined from filtering method (see section 3 for details on each method).

cases (~40% of the faults), to properly isolate the largest scale displacement fluctuations without mixing them with high-frequency oscillations, we have filtered the profiles with a cutoff frequency equal to the spatial frequency with maximum S-transform amplitude, plus three (i.e., cutoff frequency of four or five).

We have then derived the filtered fault displacement profiles to locate the null displacement gradients indicative of the points of local maximum and local minimum displacement (supporting information Figure S2d). The even positions of the null gradients indicate the major displacement troughs that separate the major segments, and their determination thus allows the precise spatial identification of the major segments along the faults. Because a filtered profile inherently differs slightly from the original profile, we had to adjust the locations of the displacement troughs onto the original profiles (supporting information Figures S2e and S2f).

This low-pass filtering allowed us to identify and isolate all major segments within each of the ~900 faults (supporting information Figure S2g), and in so doing, to precisely locate their position within the fault, their length, their individual displacement-length profile, and the maximum displacement each has accommodated (supporting information Figure S2h). We ended up with a population of ~2900 major segments.

We then similarly applied the S-transform and the low-pass filter to the ~2900 major segment displacement profiles (supporting information Figures S2i–S2l and additional example in supporting information Figure S3). As we explain further below, the S-transform analysis of the ~2900 major segment profiles revealed that, as for faults, most major segments include a similar number of secondary segments, in the range of two to five (examples in Figure 4c and supporting information Figures S2i–S2l and S3). Therefore, we could process the major segment displacement profiles in a similar way to how we treated those on faults, using the same cutoff frequencies as described before (supporting information Figures S2i–S2l and S3). However, because the displacement fluctuations on major segments might be small locally and hence at the limit of the vertical resolution of the topographic data, we have ignored the displacement fluctuations lower than 4 and 1 m for the Afar and the Asal-Ghoubbet major segments, respectively. The processing of the ~2900 major segment profiles allowed us to isolate and analyze ~6000 secondary segments.

Both methods have strengths and weaknesses. One weakness is that both techniques may fail to properly describe the characteristics of a few displacement profiles within the entire collection. We have visually

examined the ~900 fault displacement profiles, and have compared the major segments inferred from visual inspection to those identified from both methods. We found a generally good agreement between visual and signal-processing results (e.g., Figure 4). Approximately 30% and 8% of the fault displacement profiles do not seem completely described by the S-transform and by the filtering methods, respectively. The discrepancies with the S-transform method mostly arise (1) from our restrictive use of the frequency with the maximum amplitude, i.e., the assumption of segments with a similar length within each fault, and (2) from the mixing of information related to the major and the secondary segmentation. The collection of ~2900 major segment displacement profiles was too large to be visually inspected. We anticipate that the proportion of major segment cases not fully described with the S-transform and the filtering methods might be similar to that of the fault cases. On the other hand, one strength of using two signal processing techniques is that, when uniformly applied to a dense population as is the case here, they succeed in revealing robust, statistical properties of the displacement profiles. Furthermore, they provide independent results that can be compared to better assess the robustness of the findings. We prefer the low-pass filtering method as it seems more robust (better agreement between results and visual inspection), and as it provides additional information about the along-strike position, the length and the displacements of the fault segments.

4. Data Analysis

4.1. Major Segments Within Faults

4.1.1. Number of Major Segments Within Faults

We compare the distribution of the numbers of major segments (N) derived from the S-transform (Figure 5a) with the distribution from the low-pass filtering (Figure 5b) method for the entire fault population. The S-transform plot shows an approximate exponential decrease in the major segment number, from a dominant peak for $N = 2$ down to insignificant subsets for $N \geq 10$. More precisely, ~6% of the faults do not show any clear major segmentation ($N = 1$), ~36% seem to be divided into two major segments, ~16% into three major segments, ~10% into four major segments, and ~8% into five major segments. The remaining ~24% of the faults have six major segments or more. Therefore, overall, ~70% of the faults are divided into two to five major segments. A similar result is found with the filtering method (Figure 5b): more than 90% of the faults are divided into two to five major segments. These findings are consistent with the prior results of *Manighetti et al.* [2009]. The two plots differ however on the proportion of faults divided into only two major segments (~36% from S-transform, and ~20% from filtering). This difference arises from the S-transform approach being less powerful in identifying all the major segments within a fault. As a matter of fact, a large number of the profiles found to be divided into two major segments with the S-transform approach, appear to have more than only two segments, well revealed with the filtering method and from visual inspection of the profiles (see examples in supporting information Figures S5a and S5b). Similarly, a significant proportion of the fault displacement profiles classified as "unsegmented" with either the S-transform or the filtering approach actually show a fairly clear large-scale segmentation (see examples in supporting information Figures S5c and S5d).

We have verified that the results are similar regardless of geographic location, DEM resolution, fault length being less or greater than the seismogenic crust thickness, or envelope shape of the fault displacement profile (supporting information Figures S6–S8, respectively). Therefore, independent of their location, length and overall displacement distribution, about 90% of faults in the Afar region include only two to five major segments (Figure 5b).

The number of major segments within faults (here inferred from filtering method) slightly varies however as a function of the maximum displacement to length ratio of the faults (Figure 6a; see supporting information Figure S9a for a similar figure from S-transform approach). The maximum displacement to length ratio of a fault measures the amount of displacement accumulated per unit of length generally over the whole fault history, and hence it qualifies the structural maturity of a fault [e.g., *Manighetti et al.*, 2007]. We find that the number of major segments within faults linearly decreases as the fault structural maturity increases (Figure 6a). This is likely due to major segments linking together over time (Figure 1a).

4.1.2. Length and Displacement Properties of Major Segments, and Relationships With Fault Properties

The major segment lengths are in the range 0.1–36 km, whereas their maximum displacements vary between a few meters and ~1 km (supporting information Figure S10). Because the number of major

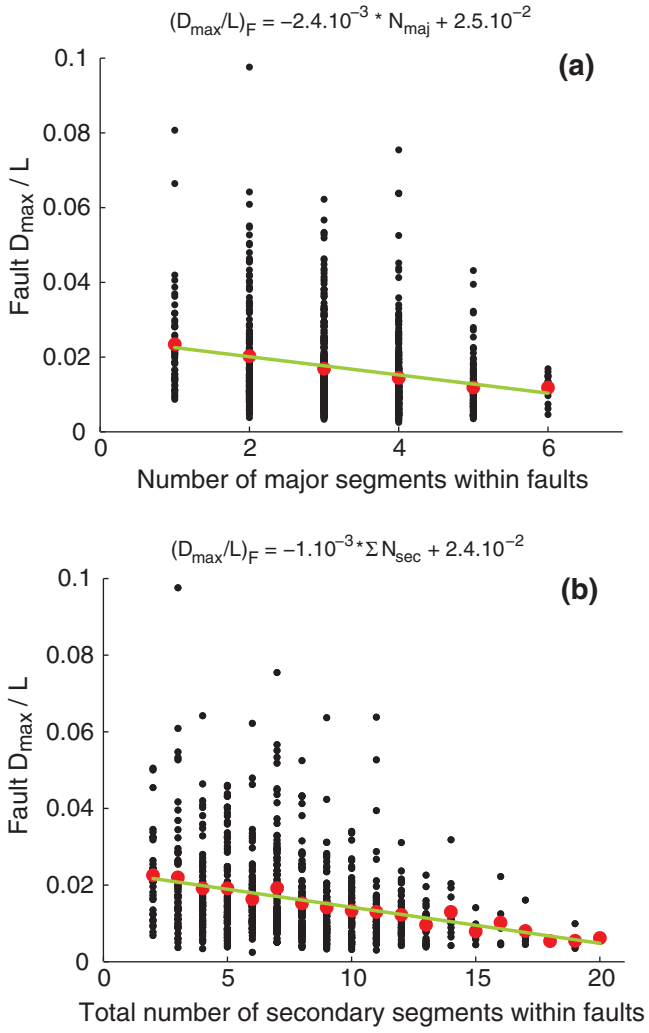

Figure 6. Number of major and secondary segments as a function of maximum displacement to length ratio of faults for the entire fault population. In the two plots, the number of segments is inferred from the filtering method. See supporting information Figure S9 for similar figures with segment number inferred from S-transform method. In both plots, individual data are in black circles, their average values are in red, and the linear regression (green line) is the calculated fit to average values. (a) Number of major segments within faults (Nmaj) as a function of maximum displacement to length ratio of the faults (Dmax/L)F (R = 0.99). (b) Total number of secondary segments within faults (SumNSec) as a function of maximum displacement to length ratio of the faults (Dmax/L)F (R = 0.98).

segments within faults is similar among faults regardless of their length, the length of the major segments varies across the fault population.

We examine the overall relation between the length of the faults and that of their major segments (Figure 7a). A linear regression fit to these data shows that, on average, regardless of the fault length, the length of the major segments is about one-third of the length of the fault they belong to. This confirms that the majority of the faults contain three major segments (see Figure 5b), whereas the major segments within a fault have a fairly similar relative length. To refine this finding, we examine the ratios of the major segment lengths (L_{SegtI}) to their master fault length (L_F), discriminating the fault cases with two, three, four, and five major segments (N, number of major segments; Figures 8a–8d). In each subset, 50–60% of the major segments have a length equal to L_F/N ± 30% (i.e., 0.5 ± 0.15 for N = 2, 0.33 ± 0.1 for N = 3, 0.25 ± 0.075 for N = 4, 0.20 ± 0.06 for N = 5).

Although major segments within faults are connected to one another and hence are no longer isolated, independent faults, overall their maximum displacement increases linearly as a function of their length, as observed for faults (compare Figures 9 and 3c).

4.1.3. Displacement Deficit at Major Intersegments as a Function of Fault Structural Maturity

For each fault having an asymmetric triangular displacement profile (i.e., degree of asymmetry ≥65%; ~50% of the faults; supporting information Figure S4), we have measured the cumulative displacement in each major displacement trough that separates two major segments (Figure 10, inset). We report these intersegment displacements normalized to the maximum fault displacement, as a function of the intersegment position along the fault, with the major segments ordered in the direction of overall displacement decrease (Figure 10). The direction of overall cumulative displacement decrease has been shown to indicate the direction in which the fault has been propagating laterally over its whole history [*Manighetti et al.*, 2001a, 2001b]. Displacement accommodated in major intersegment zones is observed to decrease in the direction of long-term fault propagation (Figure 10). Thus the displacement at major intersegments is less between younger and poorly connected segments, and displacement increases as major segments connect to each other.

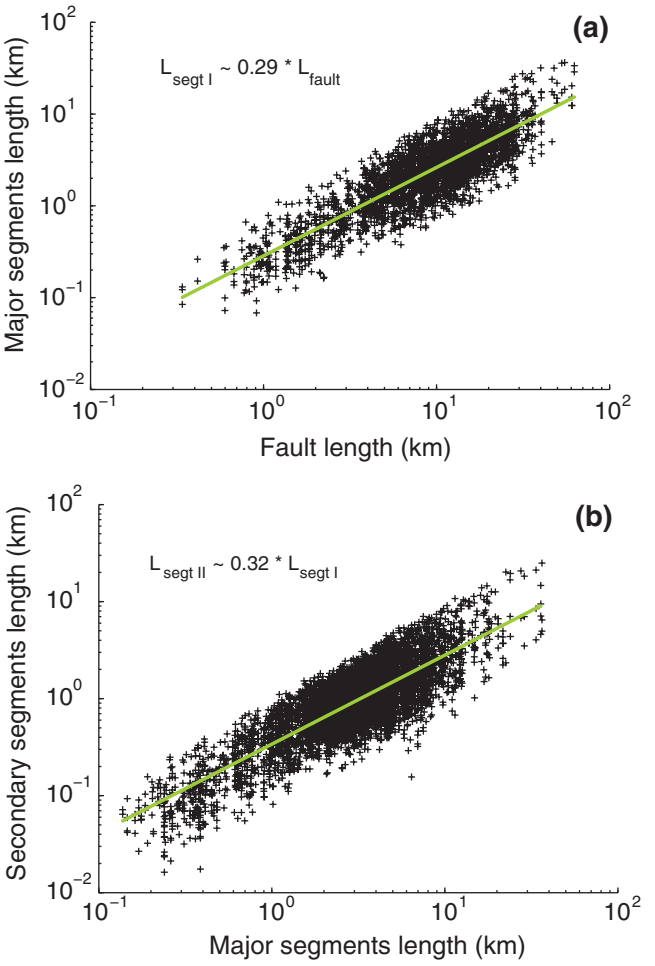

Figure 7. (a) Major segment length (LSegt I) as a function of fault length (LF) and (b) secondary segment length (LSegt II) as a function of major segment length (LSegt I), for entire fault and major segment populations. Linear regression scaling relations are in green. In (a), the linear correlation coefficient R is 0.74; a power law LSegtI ~0.030 * (Lfault)0.95 fits the data equally well (linear correlation coefficient between log(xi) and log(yi) R = 0.74). In (b), the linear correlation coefficient R is 0.74; a power law LSegtII ~0.032 * (Lfault)0.95 fits the data equally well (linear correlation coefficient between log(xi) and log(yi) R = 0.74).

A linear regression is found that relates the cumulative displacement amount at an intersegment and its position along the fault (Figure 10).

4.2. Secondary Segments Within Major Segments and Within Faults

4.2.1. Number of Secondary Segments Within Major Segments and Within Faults

We compare the distribution of the numbers of secondary segments (N_{Sec}) within major segments as derived from the S-transform (Figure 11a) and from the low-pass filtering (Figure 11b) methods for the entire major segment population. As for major segments (Figure 5a), the S-transform plot shows an approximate exponential decrease in the secondary segment number, from a dominant peak for $N_{Sec} = 2$ down to insignificant subsets for $N > 9$. More precisely, ~8% of the major segments do not show any clear secondary segmentation ($N = 1$), ~44% seem to be divided into two secondary segments, ~18% into three secondary segments, ~10% into four secondary segments, ~7% into five secondary segments, and ~4% into six secondary segments. The remaining ~9% of the major segments have seven secondary segments or more. Therefore, overall, ~80% of the major segments are divided into two to five secondary segments, and of more significance, ~70% of the major segments are divided into two to four secondary segments. A similar result is found with the filtering method (Figure 11b): whereas ~28% of the major segments seem to be unsegmented, ~70% of the major segments appear divided into two to four secondary segments (~34% into two secondary segments, ~24% into three secondary segments, ~12% into four secondary segments, and ~3% into five secondary segments). As discussed before, the S-transform approach is less powerful in discriminating the secondary displacement fluctuations. This is likely why a large number of segment profiles appear divided into two secondary segments only with the S-transform approach, whereas that number is lower when it is derived from filtering. Conversely, the filtering method fails to discriminate the secondary displacement fluctuations in some of the segment profiles, resulting in an apparently large number of "unsegmented" segment profiles. While some of these unsegmented profiles are indeed lacking clear displacement fluctuations (see examples in Figure 4, faults A16 (segment 4) and S1300 (segment 3)) or have displacement fluctuations lower than the relative vertical uncertainty on the topographic data, a significant proportion of these segment profiles actually show fairly clear secondary displacement oscillations (see examples in Figure 4, faults A16 (segment 3), A54 (segment 2), and G15 (segment 1; see also supporting information Figure S3)). Therefore, the actual number of unsegmented major segment profiles is likely to be less than suggested by the low-pass filtering results (Figure 11b).

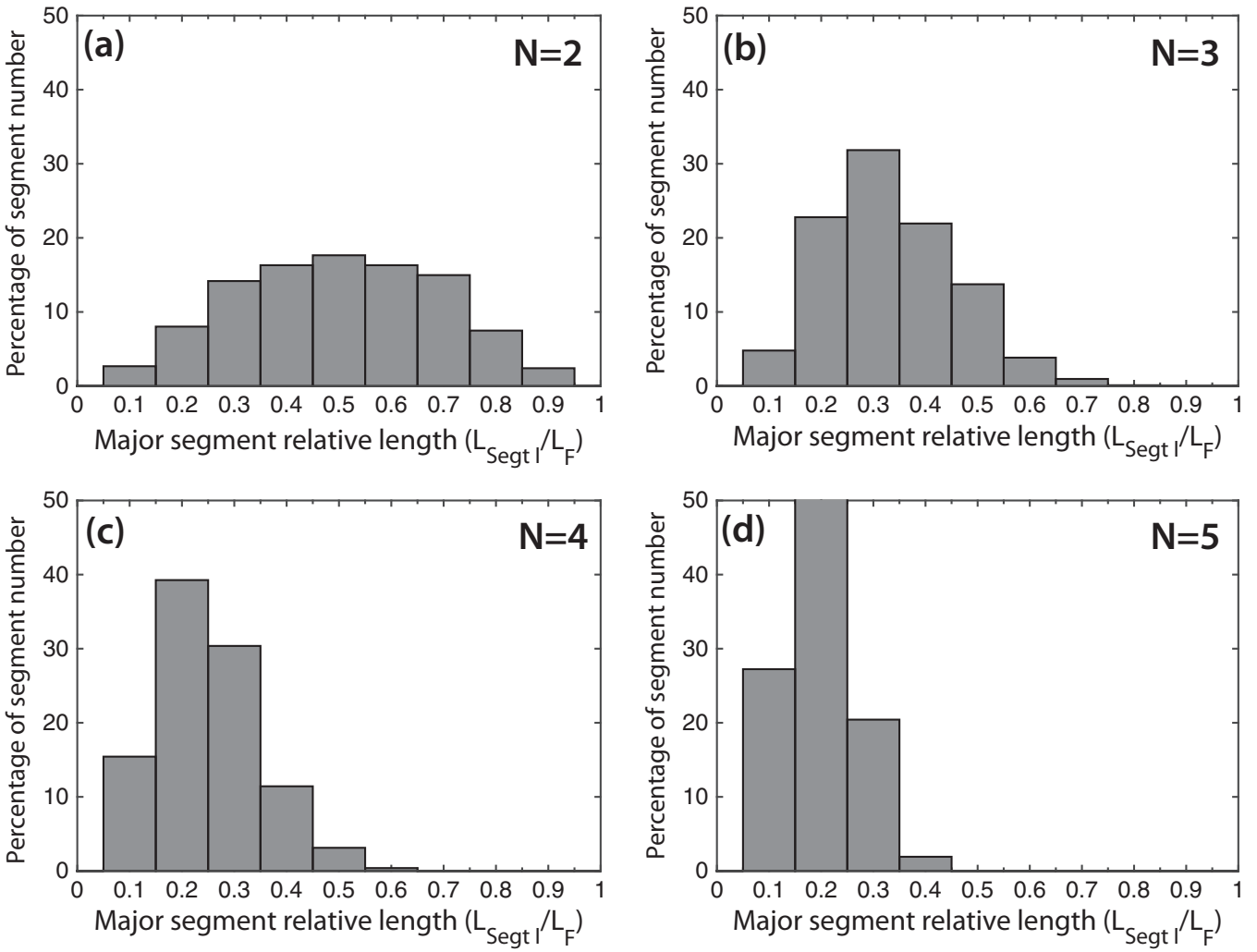

Figure 8. Distribution of the major segment lengths (LSegt I) relative to their master fault lengths (LF), for faults discriminated by their number N of major segments. (a–d) Faults having 2, 3, 4, and 5 major segments, respectively.

We have verified that the results are similar regardless of geographic location of the master fault, fault length being less or greater than the seismogenic crust thickness, or envelope shape of the master fault displacement profile (supporting information Figures S11–S13, respectively). Therefore, independent of the location, length, and overall displacement distribution of the faults they belong to, most major segments include only two to five, and more commonly two to four, secondary segments.

The total number of secondary segments within faults (inferred from filtering method) slightly decreases however as the fault displacement to length ratio and hence the fault structural maturity increases (Figure 6b; see supporting information Figure S9b for a similar figure from S-transform approach). A linear regression describes the scaling between the fault displacement-length ratio and the total number of secondary segments within that fault.

Overall, independent of their length, most faults contain five to nine secondary segments (supporting information Figure S14b, only subsets representing $\geq\sim$10% of the total population are considered; see supporting information Figure S14a for a similar figure from S-transform approach). This higher number of secondary segments within individual faults is expected, as faults typically consist of two to five major segments, which each commonly consists of two to four secondary segments.

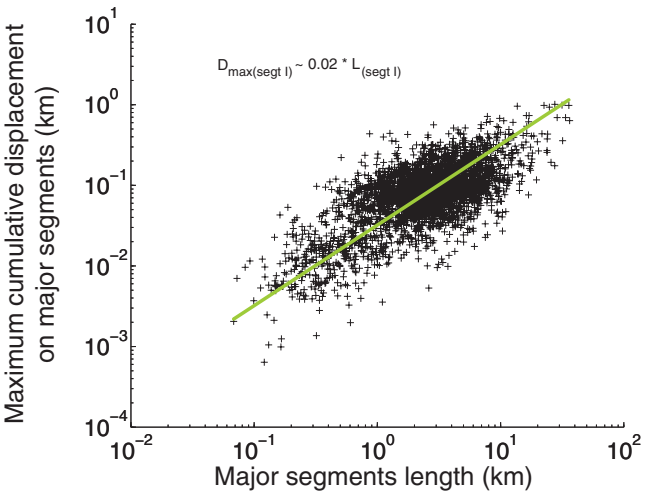

Figure 9. Scaling between maximum cumulative displacement and length of major segments. The linear scaling relation is in green. The linear correlation coefficient R is 0.61. A power law DmaxSegtl ~0.04 * (LSegtl)0.7 fits the data equally well (linear correlation coefficient between log(xi) and log(yi) R = 0.61).

4.2.2. Length Properties of Secondary Segments

While the length of the secondary segments inferred from the filtering method is meaningful, the maximum displacement that can be measured on the secondary segments is more difficult to interpret as it results from both the evolution of the secondary segments and that of the overall fault they belong to. For this reason, we do not discuss the maximum displacement values for the secondary segments.

The secondary segment lengths are in the range 0.02–20 km (see supporting information

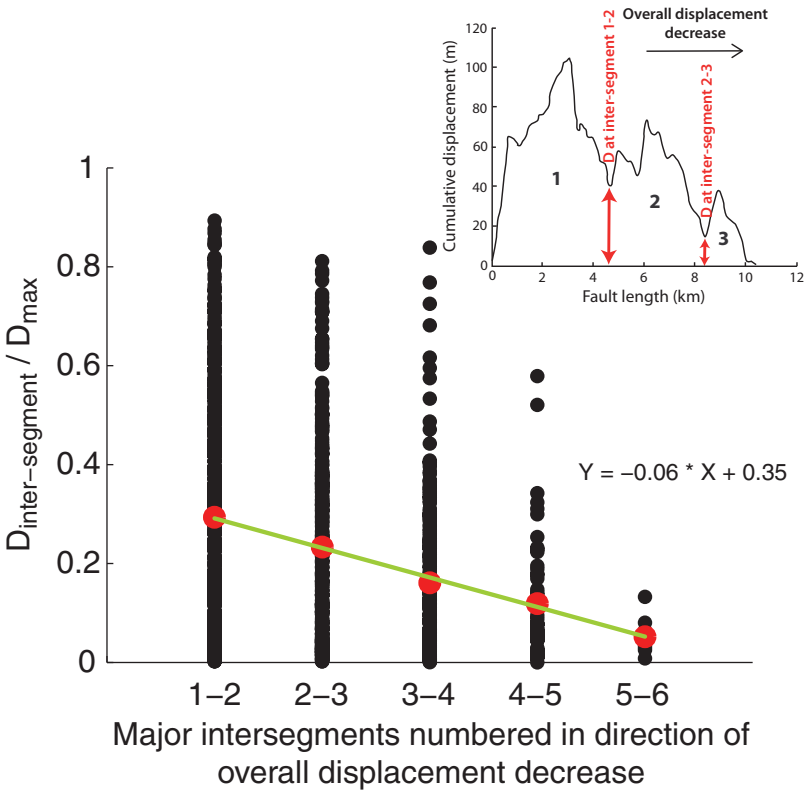

Figure 10. Relative displacement at major intersegments, in relation with their position along the fault. Only the faults having a triangular asymmetric displacement profile are considered (degree of asymmetry of best-fitting triangular function ≥65% of fault length). The major segments and hence intersegments are ordered in direction of overall cumulative displacement decrease (see inset). "1–2" on the *x* axis is thus the numbering of the major intersegment that separates the major segments 1 and 2. The inset also shows how the cumulative displacement is measured in the major intersegments (Dat intersegment). On the graph, the intersegment displacement is normalized to the maximum fault displacement. Individual data are in black, their average values in red, and a linear regression (green line, R = 0.99) is calculated from the average values.

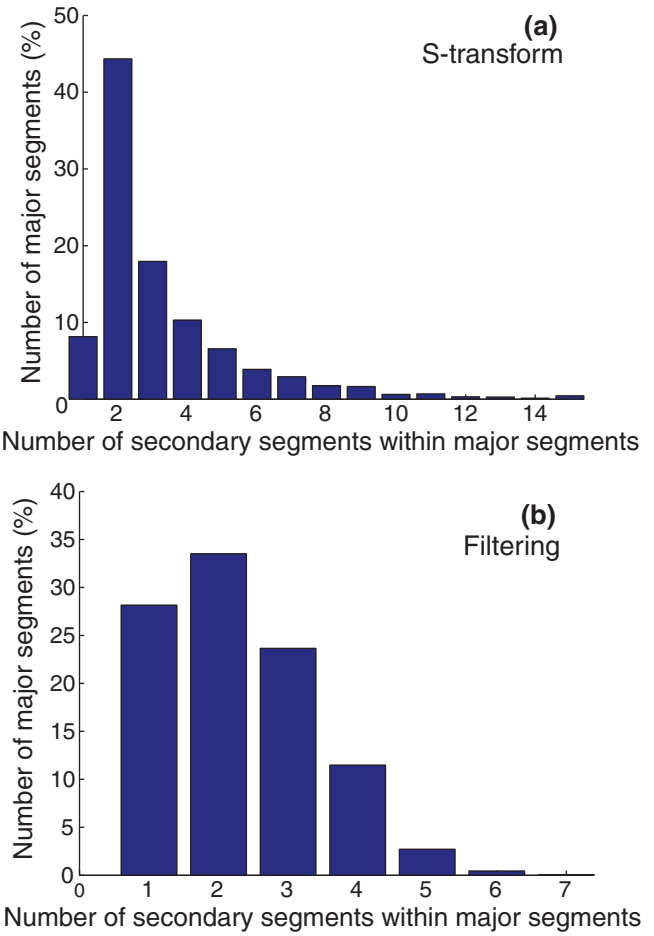

Figure 11. Distribution of the number of secondary segments within major segments for the entire major segment population (~2900). (a) determined from S-transform method; (b) determined from filtering method (see section 3 for details on each method).

Figure S15). Similar to major segments, because the number of secondary segments within major segments is similar (i.e., two to four) among most major segments regardless of their length, the length of the secondary segments differs throughout the major segment population.

We examine the overall relation between the length of the major segments and that of their secondary segments (Figure 7b). On average, the length of the secondary segments is about a third of the length of the major segment they belong to. This confirms that a large number of major segments within faults contain three secondary segments (see Figure 11b), whereas the secondary segments within a major segment have a fairly similar relative length. To refine this finding, we examine the ratios of the secondary segment lengths (L_{SegtII}) to their master major segment length (L_{SegtI}), discriminating the major segment cases with two, three, four, and five secondary segments (N_{Sec}, number of secondary segments; Figures 12a–12d). In each subset, 50–62% of the secondary segments have a length equal to $L_{SegtI}/N_{Sec} \pm 30\%$ (i.e., 0.5 ± 0.15 for $N_{Sec} = 2$, 0.33 ± 0.1 for $N_{Sec} = 3$, 0.25 ± 0.075 for $N_{Sec} = 4$, 0.20 ± 0.06 for $N_{Sec} = 5$).

5. Discussion

5.1. Comparing Segmentation of Afar Faults With Other Fault Systems

We found that the Afar normal faults are segmented along-strike at least at their two largest scales, and each of which has generic properties: independent of the fault length, location, age, slip rate, overall shape of displacement distribution, ≥90% of the faults contain a similar number of major segments, in the range of two to five (Figure 5b), whereas ≥70% of these major segments contain a similar number of subordinate, secondary segments, in the range of two to four (Figure 11b). We have compiled the published numbers and lengths of fault segments for 22 normal faults worldwide (Table 1). These segments were identified either from the geometry of the surface fault traces, or from the cumulative displacement distributions. Most reported segments are "major segments" as defined in this study, but three studies [*McLeod et al*., 2000; *Mirabella et al*., 2005; *Lohr et al*., 2008] also report subordinate scales of segmentation. The faults have different lengths (in range 0.6–350 km), ages, slip rates and they developed in different tectonic and geological settings. Yet, despite these differences, about 80% of the faults have a number of major segments in the same narrow range, of two to four, whereas the remaining ~20% of the faults have six to seven major segments. Therefore, many normal fault systems are segmented at their largest scale in a similar way as are the Afar normal faults. The three studies on subordinate segmentation show furthermore that the major segments are divided into a similar number of secondary segments, in the range of two to four (Table 1). This observation is similar to the secondary segmentation pattern we described on Afar faults.

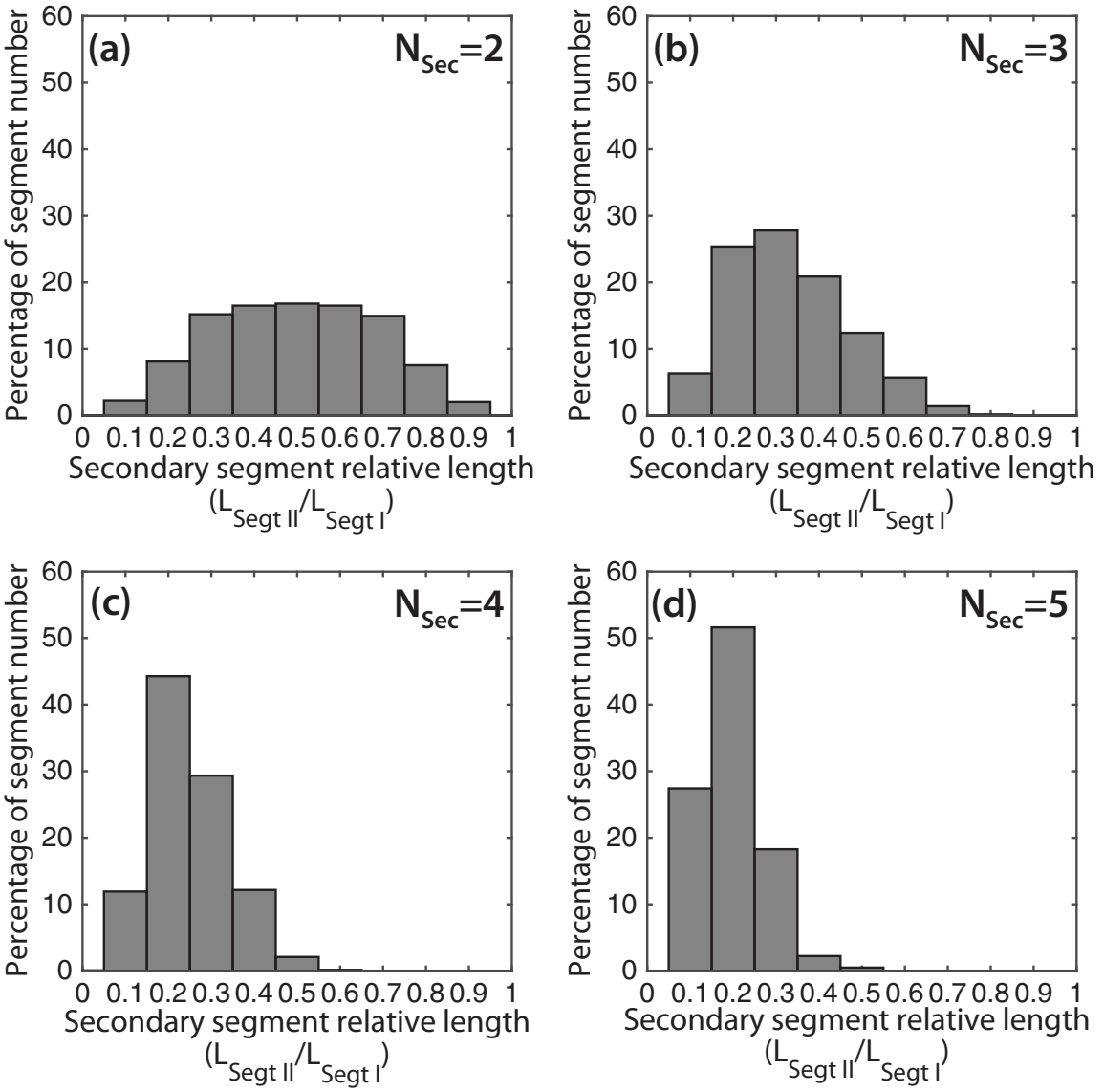

Figure 12. Distribution of the secondary segment lengths (LSegt II) relative to their master major segment lengths (LSegtI), for major segments discriminated by their number NSec of secondary segments. (a–d) Major segments having 2, 3, 4, and 5 secondary segments, respectively.

We also found that, because the number of major and of secondary segments is similar within Afar faults and major segments, respectively, their length is not, and rather increases with the fault length (Figure 7). A summary of 22 normal faults across the world shows a similar overall behavior (Table 1). The Afar data additionally show that more than 50% of the major and of the secondary segments have a length approximately equal to the fault or the major segment length divided by the number of major or of secondary segments, respectively. Most segments in other normal fault systems have a similar proportional length (Table 1) although some variability exists, as observed for the Afar faults.

We also summarize the along-strike segmentation of 7 reverse and 13 strike-slip faults worldwide that have different lengths, ages, slip rates and that developed in different tectonic and geological settings (Table 1). We are aware that fault mechanics differs between normal, reverse, and strike-slip faults [e.g., *Scholz*, 2002 and references therein], but we find interesting to compare the way these different fault types are segmented horizontally at their largest scale. The segments (Table 1) were generally identified from the geometry of the surface fault traces, especially in the strike-slip fault cases, but some were derived from displacement analysis. In all cases, the reported segments are "major segments" as defined in this study.

Table 1. Number and Length of Major and Secondary Segments Reported on 42 Faults Worldwide

Type of Fault	Fault Name (Length in Bracket)	Reported Number of Major Segments (Length in Bracket)	Reported Number of Secondary Segments (Length in Bracket)	Reported Number of Third-Order Segments (Length in Bracket)	References
Normal Faults	Arley fault at Nook colliery, UK (~1.4 km)	**3** (~0.5, 0.4, 0.7 km)			*Walsh and Watterson* [1990]
	Beaverhead Fault, US (~150 km)	**6** (~25, 42, 21, 23, 20, 20 km)			*Crone and Haller* [1991]
	Campo Felice, Italy (~12 km)	**2** (~6 and 6 km)			*Benedetti et al.* [2013]
	Colfiorito, Italy (~35 km)	**4** (~8, 9.3, 8.2, 10 km)	Segt 1: **2** Segt II? (~3, 5 km) Segt 2: 6 Segt II but **3** collinear (~4.2, 6.3, 2.6 km) Segt 3: **1** Segt II (~8.2 km) Segt 4: **1** Segt II?		*Mirabella et al.* [2005]
	Fiamignano, Italy (~15 km)	**2** (~6 and 6 km)			*Benedetti et al.* [2013]
	Lehmi Fault, US (~150 km)	**6** (~20, 29, 43, 12, 23, 23 km)			*Crone and Haller* [1991]
	Lost River Fault, US (~140 km)	**6** (~25, 29, 22, 21, 18, 25 km)			*Crone and Haller* [1991]
	No name, NW German Basin (~13 km)	**2** (~5 and 9 km)	Segt 1: **2** Segts II (~4 and 1.5 km) Segt 2: **4** Segt II (~1.5, 2.5, 1.5, 3.5 km)	Segt1_1: **4** Segt III (~2.5, 0.7, 0.4, 0.5 km) Segt1_2: **3** Segt III (~0.6, 0.5, 0.3 km) Segt2_1: **3** Segt III (~0.4, 0.4, 0.7 km) Segt2_2: **6** Segt III (~0.4, 0.8, 0.2, 0.3, 0.5, 0.6 km) Segt2_3: **3** Segt III (~0.4, 0.3, 0.6 km) Segt2_4: **5** Segt III (~0.4, 0.5, 0.3, 0.8, 1.4 km)	*Lohr et al.* [2008]
	No name, Bishop Tuff fault, US (~0.6 km)	**7** (~0.15, 0.14, 0.08, 0.13, 0.05, 0.14, 0.06 km)			*Willemse* [1997]
	No name, Bishop Tuff fault, US (~6.7 km)	**4** (~2.2, 2.6, 1.6, 2.6 km)			*Dawers and Anders* [1995]
	Parasano, Italy (~20 km)	**3** (~10, 3, 7 km)			*Benedetti et al.* [2013]
	Pleasant Valley fault, US (~60 km)	**4** (~9, 35, 7, 10 km)			*Ferrill et al.* [1999]; *De Polo et al.* [1991]
	Rangitaiki fault, New Zealand (~20 km)	**4** (~10, 5, 4, 4 km)			*Bull et al.* [2006]
	Red Rock fault, US (50–60 km)	**3** (10–15, 12, 8–10 km)			*Harkins et al.* [2005]
	San Sebastiano, Italy (~40 km)	**4** (~15, 6, 10, 10 km)			*Benedetti et al.* [2013]
	South Oquirrh Mountains fault, US (~25 km)	**4** (~6, 5, 10, 8 km)			*Wu and Bruhn* [1994]
	Strathspey-Brent-Statford fault, North Sea (~20 km)	**4** (~8, 5, 4, 4 km)	Segt 1: **2** Segts II? (~4 and 3 km) Segt 2: **3** Segt II (~2, 2, 0.8 km) Segt 3: **3** Segt II (~2, 0.5, 1.2 km) Segt 4: **2** Segt II (~2, 1.8 km)		*McLeod et al.* [2000]
	Trasacco, Italy (~35 km)	**4** (~10, 5, 7, 12 km)			*Benedetti et al.* [2013]
	Tre Monti, Italy (~20 km)	**3** (~7, 7, 7 km)			*Benedetti et al.* [2013]
	Velino-Magnola, Italy (~45 km)	**4** (~7, 7, 15, 15 km)			*Benedetti et al.* [2013]
	Wasatch fault zone, US (~350 km)	**6** to **10**, depending on authors (each ~40 to 60 km)			*Schwartz and Coppersmith* [1984] and *Machette et al.* [1991]
	Watson Draw fault, US (~12 km)	**4** (~5, 2.5, 2.5, 4.5 km)			*Crider and Pollard* [1998]

Table 1. (continued)

Type of Fault	Fault Name (Length in Bracket)	Reported Number of Major Segments (Length in Bracket)	Reported Number of Secondary Segments (Length in Bracket)	Reported Number of Third-Order Segments (Length in Bracket)	References
Reverse faults	Benmore fault, New Zealand (>2.2 km)	**2** (∼1.6, >0.5 km)			*Davis et al.* [2005]
	Chelungpu fault, Taiwan (∼90 km)	**3** (∼30, 25, 30 km)			*Simoes et al.* [2014]
	El Asnam fault, Algeria (∼30 km)	**3** (∼12, 10, 10 km)			*King and Yielding* [1984]
	Glastone fault, NZ (∼1.6 km)	**4** (∼0.2, 0.4, 0.4, 0.8 km)			*Davis et al.* [2005]
	LongmenShan Thrust Belt, China (∼450 km)	**3** (∼125, 120, 185 km)	Segt 1: **3** Segt II (∼45, 40, 40 km) Segt 2: **2** Segt II (∼70, 50 km) Segt 3: **4** Segt II (∼70, 40, 45, 30 km)		*Jin et al.* [2010]
	Ostler fault zone, New Zealand (∼35 km)	**5** (∼5, 4, 12–14, 5–6, 5 km)			*Davis et al.* [2005]
	Puente Hills fault, US (∼35 km)	**3** (∼18, 12, 10 km)			*Shaw et al.* [2002]
Strike-slip faults	Northern Altyn Tagh fault, China (∼350 km)	**4** (∼70, 95, 100, 90 km)			*Mériaux et al.* [2005]
	Southern Altyn Tagh fault, China (∼360 km)	**3** (∼200, 60, 100)			*Mériaux et al.* [2005]
	East Lut Fault, Iran (∼700 km)	**5** (∼120, 200, 150, 180, 200 km)			*Walpersdorf et al.* [2014]
	Garze-Yushu fault, China (∼500 km)	**3** (∼150,150, 300 km)	Segt 1: **1** Segt II? Segt 2: **2** Segt II (∼70, 80 km) Segt 3: **3** Segt II (∼75, 150, 75 km)		*Li et al.* [2012]
	Gemini fault, US (∼9 km)	**3** (∼3.5, 2.5, 3 km)			*Pachell and Evans* [2002]
	Gipsy point fault, Scotland (∼0.012 km)	**4** (∼0.03, 0.015, 0.04, 0.07 km)			*Peacock* [1991]
	Karakorum fault, China (∼1500 km)	**6** (∼274, 407, 265, 185, 153, 370 km)			*Chevalier et al.* [2012]
	Kunlun fault, China (∼1600 km)	**6** (∼270, 160, 210, 155, 270, 260 km)			*Van Der Woerd et al.* [2002]
	North Anatolian fault, Turkey, >1000 km	**5** (as defined by zones ruptured in largest earthquakes)			*Barka and Kadinsky-Cade* [1988] and *Barka et al.* [2002]
	Owens Valley fault, US (∼120 km)	**3** (∼60, 55, 23 km)			*Bacon and Pezzopane* [2007]
	Qujiang fault, China (∼70 km)	**2** (∼50, 20 km)			*Wang et al.* [2014]
	San Andreas fault, US (∼1000 km)	**4** (as defined from characteristic earthquake behavior, and excepting the creeping zone)			*Aviles et al.* [1987]
	San Jacinto fault, US (∼200 km)	**3** (∼80, 100, 70 km)			*Marliyani et al.* [2013]

Although the reverse faults are few (Table 1), all appear segmented at their largest scale into two to five major segments only, similar to that observed on Afar and other normal faults. Furthermore, most major segments have a fairly similar relative length.

Similarly, more than 80% of the strike-slip faults are divided into a similar number of major segments, in the range of three to five (Table 1). Most of these major segments have a fairly similar relative length. The segmentation of strike-slip faults into three to five major segments appears to be a common feature since no large historic earthquake has ever ruptured more than three major intersegments on a strike-slip fault [*Wesnousky and Biasi*, 2011]. In their laboratory experiment aimed at investigating the growth of strike-slip faults, *Otsuki and Dilov* [2005] observed that the along-strike fault segmentation could be ranked in a hierarchical sense, with the number of segments in any given hierarchical rank ranging from two to five. *de Joussineau*

and Aydin [2009] made the same observation from a dense population of natural strike-slip faults, and concluded that, regardless of their environment, strike-slip faults have a remarkable self-similar architecture. Altogether these observations suggest that, although they obey a different mechanics from dip-slip faults, strike-slip faults are segmented along their trace in a similar way as dip-slip faults.

5.2. Implications on Fault Growth Processes

A major implication of normal fault segmentation being generic and similar, at least at its two largest scales, is that the process through which normal faults become horizontally segmented is not random, but rather must be an intrinsic outcome of the fault growth process. Therefore, it is unlikely that major and secondary segments within normal faults form randomly or simultaneously as it has been commonly suggested [e.g., *Anders and Schlische*, 1994; *Cartwright et al*., 1995; *Childs et al*., 1995; *McLeod et al*., 2000; *Cowie and Roberts*, 2001; *Young et al*., 2001; *Walsh et al*., 2003 for normal faults; see also *Segall and Pollard*, 1980; *Kim et al*., 2004; *Davis et al*., 2005 for other fault types]. Rather, they might form as a result of the fault growth in space and time (as recognized by *Giba et al*. [2012]). Similar to previous findings [on all fault types, e.g., *Walsh and Watterson*, 1988; *Cowie and Scholz*, 1992; *Dawers et al*., 1993; *Schlische et al*., 1996; *Manighetti et al*., 2001a, 2001b; *Scholz*, 2002; *Davis et al*., 2005], we show that there is a maximum displacement to length ratio ($D_{max}/L \sim 0.1$) above which a normal fault with a given length does not accumulate further slip while maintaining its length (Figure 3c, dotted line). This observation implies that a normal fault grows over the long-term through alternating phases of dominant displacement accumulation possibly at constant length [e.g., *Nicol et al*., 2005; *Bull et al*., 2006; *Giba et al*., 2012], by the end of which its displacement to length ratio reaches the observed ~0.1 threshold value, and of dominant lateral propagation, possibly with little displacement increase, during which the fault lengthens and therefore its D_{max}/L ratio drops down. The times of displacement accumulation at fairly constant length have been shown to be long, up to several 10^4-10^6 years [e.g., *Nicol et al*., 2005; *Bull et al*., 2006]. Furthermore, as a normal fault grows, it accumulates displacement in a generic manner (triangular asymmetric displacement-length function, observed for all fault types) while it also damages the surrounding rock volume [observed for all fault types, e.g., *Manighetti et al*., 2004; *Schlagenhauf et al*., 2008; *Cappa et al*., 2014; *Johri et al*., 2014]. Therefore, we follow *Schlagenhauf et al*. [2008] (see their Figure 10; see also similar conceptual ideas in *Wu and Bruhn* [1994], *Davis et al*. [2005], and *Aydin and Berryman* [2010]) and suggest that the fault segments are formed during the fault growth, as a result of it: as a normal fault accumulates displacement at a fairly constant length, static stresses build up around the fault, especially at its tips. These large stress concentrations contribute to damage the crust around and beyond the fault, partly in the form of new cracks and tiny faults being created or reactivated off-the main fault [e.g., *Cappa et al*., 2014 and references therein for a geological perspective; e.g., *Leblond et al*., 2011 and references therein for a theoretical perspective]. Depending on the ratio between the near fault tip stresses and the strength of the medium at the fault tips, the damage cracks may grow and coalesce to form a well defined, new individual fault, or "segment," ahead of the growing master fault. It is likely that the length of such a newly formed segment depends on the level of the near-tip stress concentration, which, in turn, depends on the length of the growing master fault. Once one or two segments are formed at one or at both tips of the growing master fault, the latter may lengthen horizontally by connecting to those segments. This process results in a longer normal fault, now made of two or three major segments, and ready to resume accumulating displacement at such a new, greater length. The process would then repeat as before, continually lengthening the fault in a punctuated manner. Traces of the original segments would remain on the fault plane in the form of narrow zones of persisting displacement deficit [e.g., *Manighetti et al*., 2001a, 2001b; *Bull et al*., 2006; *Schlagenhauf et al*., 2008]. A normal fault might continue to grow as suggested above until its length reaches the maximum possible length that is dictated by the seismogenic thickness and the effective elastic thickness of the crust it cuts through [e.g., *Scholz and Contreras*, 1998].

This conceptual vision of normal fault growth over the long-term may provide a framework to understand the scale-invariant properties of the along-strike normal fault segmentation. The scenarios described above apply to normal faults, but it is possible that they might apply as well to reverse and strike-slip faults since it is the fault lengthening process that seems to most control the along-strike segmentation.

5.3. Implications for Stress Heterogeneity on Seismogenic Normal Fault Planes

Independent of the way normal fault segments form, they produce a remarkable, deterministic horizontal division of a master fault and this deterministic division is expected to markedly control both the slip and

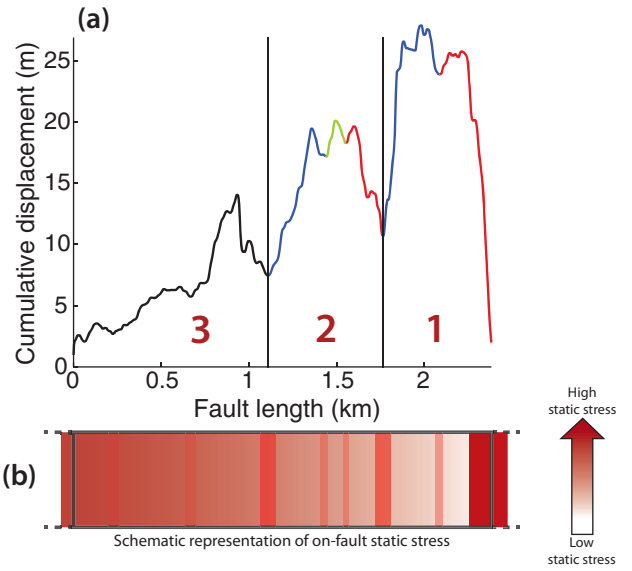

Figure 13. Schematic representation of the static stress distribution on an Afar seismogenic fault plane. (a) An example displacement-length profile of one of the analyzed Afar normal faults (from Figure 4). Three major segments are identified, numbered from right to left. Note that we consider the smaller-scale displacement fluctuations in major segment 3 as indicative of the secondary segmentation of that segment although the filtering approach did not reveal it properly. (b) Schematic representation of the corresponding fault plane (thick black contour) and of the static stress distribution on this plane. Stress is not calculated but only schematically represented. Stress increase is represented with darker red colors. The triangular and asymmetric envelope shape of the cumulative displacement-length profile produces static stresses that, overall, increase progressively from right to left of the fault plane. Because of the high displacement gradient at the right fault tip, the stress concentration at this tip is very high. The large stresses at both fault tips extend also ahead of the fault (dotted black lines). The major intersegments are additional local zones of large stress concentrations. The secondary intersegments also are additional local zones of stress concentrations, yet of smaller amplitudes than those related to the major intersegments. Note that, for clarity, we have not represented the stress variation that likely results from the major segment displacement profiles being also triangular and asymmetric overall. The fault plane thus appears punctuated with nine local spots of large stress concentrations (including those at fault tips), that add to the overall stress increase from right to left.

the static stress distribution on the seismogenic normal fault plane. We provide a schematic representation of the expected static stress distribution on an Afar normal fault plane (Figure 13). Fault cumulative displacement distributions are not stochastic but instead deterministic: the displacement-length profile of most faults has a generic, self-similar triangular asymmetric overall shape. Therefore, because static stress on fault planes is basically inversely proportional to cumulative displacement, we infer that, overall, the static stress gradually varies on a seismogenic fault plane, from being minimum in the zone of maximum cumulative displacement to being greatest at the other fault extremity where displacement tapers to zero. A high stress concentration is also expected at the fault tip with a high displacement gradient. Therefore, while the static stress distribution is heterogeneous on a seismogenic fault plane, the heterogeneity is fairly smooth. As the generic shape of the displacement distribution is observed for all types of faults, the above inference similarly applies to dip-slip and strike-slip faults.

Moreover, the Afar normal faults are segmented along-strike in a similar fashion, in two to five major segments, each is itself divided into two to four secondary segments. Afar normal faults are thus punctuated with a deterministic number of intersegment zones. Because the segments analyzed here are the longest within the faults, most are likely to be 3-D features, effectively dividing the fault plane entirely [e.g., *Segall and Pollard*, 1980]. Whether they are major or secondary, the segments terminate at locations with high displacement gradients (see Figures 4 and 13), so that high stress concentrations are expected in or at the edge of the intersegment zones (Figure 13). Therefore, the generic horizontal segmentation of faults implies that most fault planes are punctuated, in a similar manner, with concentrations of large static stress that coincide with their major and secondary intersegments (Figure 13). We did not analyze the displacement distributions on the individual major segments because it was not clear how we could compare displacement profiles that have been more or less modified depending on the degree of connection between the segments. However, a visual inspection of the major segment profiles suggests that a large number of them also show a triangular and asymmetric envelope shape (see examples in Figure 4, and segment 3 in Figure 13). Therefore, the static stress distributions on normal fault planes might show additional variations in between the major stress "spots," due to the tapered displacement distribution on the major fault segments.

Fault segmentation has been suggested to be fractal [e.g., *Scholz and Aviles*, 1986; *Okubo and Aki*, 1987; *Andrews and Barral*, 2011]. However, no study has analyzed the characteristics of fault segmentation over

several scales down to very small ones. Only studies of fault "roughness" have been conducted [e.g., *Candela et al*., 2012 and references therein], but the relationships between the different forms of fault roughness observed at surface and the actual fault segmentation have not been established. Our observation that the number of both major and secondary segments decreases slightly as a normal fault accumulates more displacement and hence as its segments become more fully connected (Figure 6), suggests that small scale segments are smoothed out during the fault evolution [see also *Wesnousky*, 1988; *Stirling et al*., 1996; *Sagy et al*., 2007; *Lohr et al*., 2008; *de Joussineau and Aydin*, 2009] and hence are not entirely preserved in the fault displacement profiles and surface traces. Therefore, there is little chance that fault segmentation be fractal beyond, perhaps, the earliest stages of the fault evolution. In turn, if fault segmentation is not fractal, the static stress distribution on seismogenic fault planes is unlikely to be as heterogeneous as it has been suggested [e.g., *Cowie and Shipton*, 1998; *Duan and Oglesby*, 2006].

The intersegments are zones of cumulative displacement deficit and this shows that, despite the high stress concentrations they sustain, the intersegments accommodate little to no on-fault displacement. Therefore, the zones that separate the major and the secondary segments do not respond as expected if elastic stresses build up during the repeated seismic cycles. It has been long known that the intersegment zones are regions of distributed and pervasive small-scale cracking and faulting [e.g., *King*, 1983; *Crider and Pollard*, 1998; *Sibson*, 2003; *Manighetti et al*., 2004; *de Joussineau and Aydin*, 2009]. The high stresses and strain might thus be dissipated among the multiple tiny features, and this dissipation might make the crust in the intersegment zones responding to stresses in a manner close to plasticity. This implies that, although the stress concentrations might be significant on the fault plane at the intersegment zones, they might be lower than expected because part of these stresses are dissipated within the 3-D, elastic-plastic intersegment volumes.

6. Conclusions

We have shown in this paper that the along-strike segmentation of the Afar normal faults is similar and generic at the two scales analyzed; regardless of their length, age, geographic location, total displacement, and slip rate, more than 90% of the faults contain a similar number of major segments, in the range of two to five (Figure 5), whereas more than 70% of these major segments also contain a similar number of secondary segments, in the range of two to four (Figure 11). The Afar normal faults are thus divided into constant-number segments, and therefore, these segments have variable absolute lengths (Figure 7). By contrast, in most faults, the segments of a given rank have a fairly similar proportional length (Figure 8). Although the number of major and secondary segments is similar overall among the faults, that number slightly decreases with the fault structural maturity (Figure 6). This is because the segments become more connected to each other as a fault accumulates more displacement. The greater connection of the segments as a fault becomes more mature is also revealed by the increase in the displacement at the major intersegments (Figure 10).

The along-strike division of the Afar normal faults is thus generic and deterministic, at least at its two largest scales. The compilation of fault segment data on normal, reverse and strike-slip faults worldwide suggests that the generic segmentation revealed for the Afar normal faults might be a general property of dip-slip faults, and even, possibly, of strike-slip faults (Table 1). This generic property of the fault horizontal segmentation is likely to be a fundamental outcome of the fault growth process. We suggest that, at some stage of fault evolution, the stress concentrations at and near the tips of a growing fault with constant length create new cracks and small faults ahead of the growing master fault. As the tip-stresses increase, these cracks might coalesce to form a new fault segment that the master fault connects to, to grow in length. This conceptual vision of fault growth and lengthening through segment creation and linkage needs to be modeled. Such modeling is complex however as it must include several ingredients: (i) a nonplanar fault; (ii) a 3-D heterogeneous medium with both elastic and likely plastic properties; (iii) the evolution of the medium and fault properties as the fault is growing and damaging the crust; (iv) an heterogeneous and evolving static stress distribution on the fault plane; (v) a likely variable friction on the fault plane, especially at intersegments; (vi) the occurrence of dynamic rupture (see partial discussions in *Noda et al*. [2013], *Cappa et al*. [2014], and *Johri et al*. [2014]).

Independent of the way large-scale fault segments form, the intersegments that separate them are zones of stress concentrations, and they also are zones with mechanical and friction properties different from those

of the rest of the fault [e.g., *Sibson*, 1986; *Kaneko et al*., 2010; *Johri et al*., 2014]. Furthermore, the cumulative displacement deficits at major intersegments persist over long times [$>10^4-10^6$ years; present study and e.g., *Nicol et al*., 2005; *Bull et al*., 2006], and this shows that intersegments are persisting "barriers" to fault slip. Because most are zones of distributed cracking, they might be "weak barriers," i.e., zones capable of sustaining high stresses without producing much on-fault displacement [e.g., *Manighetti et al*., 2004, 2007]. Therefore, intersegments are specific zones on a fault, whose large stresses might favor earthquake nucleation [e.g., *Aki*, 1979; *Barka and Kadinsky-Cade*, 1988; *Shaw*, 2006], whereas their inelastic properties might favor earthquake arrest. The along-strike segmentation of faults is thus expected to markedly control the nucleation and the extent of earthquake ruptures. Additionally, the large stress concentrations at the intersegments are prone to favor stress transfers and hence to induce a variability in the location and the time of the different segment ruptures along a fault [e.g., *Kaneko et al*., 2010].

Acknowledgments
The DEM data used here have been acquired by the French IGN and the French IFREMER (Tadjouraden oceanographic cruise), and from the freely accessible SRTM topography (http://www2.jpl.nasa.gov/srtm). We thank two anonymous reviewers, Scott E. K. Bennett, and the Editor Thorsten Becker for their thorough and constructive comments that greatly contributed to improve the manuscript.

References

Aki, K. (1979), Characterization of barriers on an earthquake fault, *J. Geophys. Res.*, *84*(B11), 6140–6148.
Anders, M. H., and R. W. Schlische (1994), Overlapping faults, intrabasin highs, and the growth of normal faults, *J. Geol.*, *102*, 165–179.
Andrews, D. J., and M. Barral (2011), Specifying initial stress for dynamic heterogeneous earthquake source models, *Bull. Seismol. Soc. Am.*, *101*(5), 2408–2417, doi:10.1785/0120110012.
Audin, L., I. Manighetti, P. Tapponnier, F. Métivier, E. Jacques, and P. Huchon (2001), Fault propagation and climatic control of sedimentation on the Ghoubbet rift floor: Insights from the Tadjouraden cruise in the western Gulf of Aden, *Geophys. J. Int.*, *144*(2), 391–413.
Aviles, C. A., C. H. Scholz, and J. Boatwright (1987), Fractal analysis applied to characteristic segments of the San Andreas fault, *J. Geophys. Res.*, *92*(B1), 331–344.
Aydin, A., and J. G. Berryman (2010), Analysis of the growth of strike-slip faults using effective medium theory, *J. Struct. Geol.*, *32*(11), 1629–1642.
Aydin, A., and R. A. Schultz (1990), Effect of mechanical interaction on the development of strike-slip faults with echelon patterns, *J. Struct. Geol.*, *12*(1), 123–129.
Bacon, S. N., and S. K. Pezzopane (2007), A 25,000-year record of earthquakes on the Owens Valley fault near Lone Pine, California: Implications for recurrence intervals, slip rates, and segmentation models, *Geol. Soc. Am. Bull.*, *119*(7–8), 823–847.
Barka, A., et al. (2002), The surface rupture and slip distribution of the 17 August 1999 Izmit earthquake (M 7.4), North Anatolian fault, *Bull. Seismol. Soc. Am.*, *92*(1), 43–60.
Barka, A. A., and K. Kadinsky-Cade (1988), Strike-slip fault geometry in Turkey and its influence on earthquake activity, *Tectonics*, *7*(3), 663–684.
Ben-Zion, Y., and C. G. Sammis (2003), Characterization of fault zones, *Pure Appl. Geophys.*, *160*(3–4), 677–715.
Benedetti, L., I. Manighetti, Y. Gaudemer, R. Finkel, J. Malavieille, K. Pou, M. Arnold, G. Aumaître, D. Bourlès, and K. Keddadouche (2013), Earthquake synchrony and clustering on Fucino faults (Central Italy) as revealed from in situ 36Cl exposure dating, *J. Geophys. Res. Solid Earth*, *118*, 4948–4974, doi:10.1002/jgrb.50299.
Black, N. M., and D. D. Jackson (2008), Probability of multifault rupture, *Bull. Seismol. Soc. Am.*, *98*(6), 3017–3024.
Bull, J. M., P. M. Barnes, G. Lamarche, D. J. Sanderson, P. A. Cowie, S. K. Taylor, and J. K. Dix (2006), High-resolution record of displacement accumulation on an active normal fault: Implications for models of slip accumulation during repeated earthquakes, *J. Struct. Geol.*, *28*(7), 1146–1166.
Bürgmann, R., D. D. Pollard, and S. J. Martel (1994), Slip distributions on faults: Effects of stress gradients, inelastic deformation, heterogeneous host-rock stiffness, and fault interaction, *J. Struct. Geol.*, *16*(12), 1675–1690.
Butterworth, S. (1930), On the theory of filter amplifiers, *Wireless Eng.*, *7*, 536–541.
Candela, T., F. Renard, M. Bouchon, A. Brouste, D. Marsan, J. Schmittbuhl, and C. Voisin (2009), Characterization of fault roughness at various scales: Implications of three-dimensional high resolution topography measurements, *Pure Appl. Geophys.*, *166*(10–11), 1817–1851.
Candela, T., F. Renard, Y. Klinger, K. Mair, J. Schmittbuhl, and E. E. Brodsky (2012), Roughness of fault surfaces over nine decades of length scales, *J. Geophys. Res.*, *117*, B08409, doi:10.1029/2011JB009041.
Cappa, F., C. Perrin, I. Manighetti, and E. Delor (2014), Off-fault long-term damage: A condition to account for generic, triangular earthquake slip profiles, *Geochem. Geophys. Geosyst.*, *15*, 1476–1493, doi:10.1002/2013GC005182.
Cartwright, J. A., B. D. Trudgill, and C. S. Mansfield (1995), Fault growth by segment linkage: An explanation for scatter in maximum displacement and trace length data from the Canyonlands Grabens of SE Utah, *J. Struct. Geol.*, *17*(9), 1319–1326.
Chevalier, M. L., P. Tapponnier, J. Van der Woerd, F. J. Ryerson, R. C. Finkel, and H. Li (2012), Spatially constant slip rate along the southern segment of the Karakorum fault since 200 ka, *Tectonophysics*, *530*, 152–179.
Childs, C., J. Watterson, and J. J. Walsh (1995), Fault overlap zones within developing normal fault systems, *J. Geol. Soc.*, *152*(3), 535–549.
Clifton, A. E., R. W. Schlische, M. O. Withjack, and R. V. Ackermann (2000), Influence of rift obliquity on fault-population systematics: Results of experimental clay models, *J. Struct. Geol.*, *22*, 1491–1510.
Cowie, P. A., and G. P. Roberts (2001), Constraining slip rates and spacings for active normal faults, *J. Struct. Geol.*, *23*(12), 1901–1915.
Cowie, P. A., and C. H. Scholz (1992), Displacement-length scaling relationship for faults: Data synthesis and discussion, *J. Struct. Geol.*, *14*(10), 1149–1156.
Cowie, P. A., and Z. K. Shipton (1998), Fault tip displacement gradients and process zone dimensions, *J. Struct. Geol.*, *20*(8), 983–997.
Crider, J. G., and D. D. Pollard (1998), Fault linkage: Three-dimensional mechanical interaction between echelon normal faults, *J. Geophys. Res.*, *103*(B10), 24,373–24,391.
Crone, A. J., and K. M. Haller (1991), Segmentation and the coseismic behavior of Basin and Range normal faults: Examples from east-central Idaho and southwestern Montana, USA, *J. Struct. Geol.*, *13*(2), 151–164.
Das, S. (2003), Spontaneous complex earthquake rupture propagation, in *Seismic Motion, Lithospheric Structures, Earthquake and Volcanic Sources: The Keiiti Aki Volume*, pp. 579–602, Pageoph Topical Volumes, Birkhäuser Basel.
Davis, K., D. W. Burbank, D. Fisher, S. Wallace, and D. Nobes (2005), Thrust-fault growth and segment linkage in the active Ostler fault zone, New Zealand, *J. Struct. Geol.*, *27*(8), 1528–1546.

Dawers, N. H., and M. H. Anders (1995), Displacement-length scaling and fault linkage, *J. Struct. Geol.*, *17*(5), 607–614.
Dawers, N. H., M. H. Anders, and C. H. Scholz (1993), Growth of normal faults: Displacement-length scaling, *Geology*, *21*(12), 1107–1110.
De Chabalier, J. B., and J. P. Avouac (1994), Kinematics of the Asal Rift (Djibouti) determined from the deformation of Fieale Volcano, *Science*, *265*(5179), 1677–1681.
de Joussineau, G., and A. Aydin (2009), Segmentation of strike-slip faults revisited, *Pure Appl. Geophys.*, *166*(10), 1575–1594, doi:10.1007/s00024-009-0511-4.
DePolo, C. M., D. G. Clark, D. B. Slemmons, and A. R. Ramelli (1991), Historical surface faulting in the Basin and Range province, western North America: Implications for fault segmentation, *J. Struct. Geol.*, *13*(2), 123–136.
Doubre, C., I. Manighetti, C. Dorbath, L. Dorbath, E. Jacques, and J.-C. Delmond (2007a), Crustal structure and magmato-tectonic processes in an active rift (Asal-Ghoubbet, Afar, East-Africa). Part 1: Insights from a five-month seismological experiment, *J. Geophys. Res.*, *112*, B05405, doi:10.1029/2005JB003940.
Doubre, C., I. Manighetti, L. Dorbath, C. Dorbath, D. Bertil, E. Jacques, and J.-C. Delmond (2007b), Crustal structure and magmato-tectonic processes in an active rift (Asal-Ghoubbet, Afar, East-Africa). Part 2: Insights from the 23 years recording of seismicity since the last rifting event, *J. Geophys. Res.*, *112*, B05406, doi:10.1029/2006JB004333.
Duan, B., and D. D. Oglesby (2006), Heterogeneous fault stresses from previous earthquakes and the effect on dynamics of parallel strike-slip faults, *J. Geophys. Res.*, *111*, B05309, doi:10.1029/2005JB004138.
Dugdale, D. S. (1960), Yielding of steel sheets containing slits, *J. Mech. Phys. Solids*, *8*(2), 100–104.
Ellis, M. A., and W. J. Dunlap (1988), Displacement variation along thrust faults: Implications for the development of large faults, *J. Struct. Geol.*, *10*(2), 183–192.
Eshelby, J. D. (1957), The determination of the elastic field of an ellipsoidal inclusion, and related problems, *Proc. R. Soc. London, Ser. A*, *241*(1226), 376–396.
Farbod, Y., O. Bellier, E. Shabanian, and M. R. Abbassi (2011), Geomorphic and structural variations along the Doruneh Fault System (central Iran), *Tectonics*, *30*, TC6014, doi:10.1029/2011TC002889.
Farr, T. G., and M. Kobrick (2000), Shuttle radar topography mission produces a wealth of data, *Eos Trans. AGU*, *81*(48), 583–585.
Ferrill, D. A., J. A. Stamatakos, and D. Sims (1999), Normal fault corrugation: Implications for growth and seismicity of active normal faults, *J. Struct. Geol.*, *21*(8), 1027–1038.
Giba, M., J. J. Walsh, and A. Nicol (2012), Segmentation and growth of an obliquely reactivated normal fault, *J. Struct. Geol.*, *39*, 253–267.
Gorokhovich, Y., and A. Voustianiouk (2006), Accuracy assessment of the processed SRTM-based elevation data by CGIAR using field data from USA and Thailand and its relation to the terrain characteristics, *Remote Sens. Environ.*, *104*(4), 409–415.
Griffith, A. A. (1920), The phenomena of rupture and flow in solids, *Philos. Trans. R. Soc. London A*, *221*, 163–198.
Griffith, A. A. (1924), The theory of rupture, in *Proceedings of the First International Congress for Applied Mechanics*, edited by C. B. Biezeno, and J. M. Burgers, Delft: Tech. Boekhandel en Drukkeerij J. Walter Jr., pp. 53–63.
Harkins, N. W., D. J. Anastasio, and F. J. Pazzaglia (2005), Tectonic geomorphology of the Red Rock fault, insights into segmentation and landscape evolution of a developing range front normal fault, *J. Struct. Geol.*, *27*(11), 1925–1939.
Hecker, S., T. E. Dawson, and D. P. Schwartz (2010), Normal-faulting slip maxima and stress-drop variability: A geological perspective. *Bull. Seismol. Soc. Am.*, *100*(6), 3130–3147.
Johri, M., E. M. Dunham, M. D. Zoback, and Z. Fang (2014), Predicting fault damage zones by modeling dynamic rupture propagation and comparison with field observations, *J. Geophys. Res. Solid Earth*, *119*, 1251–1272, doi:10.1002/2013JB010335.
Kaneko, Y., J. P. Avouac, and N. Lapusta (2010), Towards inferring earthquake patterns from geodetic observations of interseismic coupling, *Nat. Geosci.*, *3*(5), 363–369.
Kanninen, M. F., and C. H. Popelar (1985), *Advanced Fracture Mechanics*, 573 pp., Oxford Univ. Press, N. Y.
Kase, Y. (2010), Slip-length scaling law for strike-slip multiple segment earthquakes based on dynamic rupture simulations, *Bull. Seismol. Soc. Am.*, *100*(2), 473–481.
Kim, Y. S., D. C. Peacock, and D. J. Sanderson (2004), Fault damage zones, *J. Struct. Geol.*, *26*(3), 503–517.
King, G. (1983), The accommodation of large strains in the upper lithosphere of the earth and other solids by self-similar fault systems: The geometrical origin of b-value, *Pure Appl. Geophys.*, *121*(5–6), 761–815.
King, G., and G. Yielding (1984), The evolution of a thrust fault system: Processes of rupture initiation, propagation and termination in the 1980 El Asnam (Algeria) earthquake, *Geophys. J. Int.*, *77*(3), 915–933.
King, G., and J. Nabelek (1985), Role of fault bends in the initiation and termination of earthquake rupture, *Science*, *228*(4702), 984–987.
Klinger, Y. (2010), Relation between continental strike-slip earthquake segmentation and thickness of the crust, *J. Geophys. Res.*, *115*, B07306, doi:10.1029/2009JB006550.
Klinger, Y., X. Xu, P. Tapponnier, J. Van der Woerd, C. Lasserre, and G. King (2005), High-resolution satellite imagery mapping of the surface rupture and slip distribution of the Mw$\sim$ 7.8, 14 November 2001 Kokoxili earthquake, Kunlun fault, northern Tibet, China, *Bull. Seismol. Soc. Am.*, *95*(5), 1970–1987.
Klinger, Y., T. K. Rockwell, N. Cubas, and P. Souloumiac (2013), Along strike-slip faults, do fault segments exist and how long are they?, Abstract T42A-06 presented at 2013 Fall Meeting, AGU, San Francisco, Calif.
Knuepfer, P. L. K. (1989), Implications of the characteristics of end-points of historical surface fault ruptures for the nature of fault segmentation, in edited by D. P. Schwartz, and R. H. Sibson, Fault Segmentation and Controls of Rupture Initiation and Termination, *U.S. Geol. Sur. Open-File Report* 89-315, 193–228.
Leblond, J. B., A. Karma, and V. Lazarus (2011), Theoretical analysis of crack front instability in mode I + III, *J. Mech. Phys. Solids*, *59*(9), 1872–1887.
Lettis, W., J. Bachhuber, R. Witter, C. Brankman, C. E. Randolph, A. Barka, W. D. Page, and A. Kaya (2002), Influence of releasing step-overs on surface fault rupture and fault segmentation: Examples from the 17 August 1999 Izmit earthquake on the North Anatolian fault, Turkey, *Bull. Seismol. Soc. Am.*, *92*(1), 19–42.
Li, C. Y., J. Z. Pang, and Z. Q. Zhang (2012), characteristics, geometry, and segmentation of the surface rupture associated with the 14 April 2010 Yushu Earthquake, Eastern Tibet, China, *Bull. Seismol. Soc. Am.*, *102*(4), 1618–1638.
Lohr, T., C. M. Krawczyk, O. Oncken, and D. C. Tanner (2008), Evolution of a fault surface from 3D attribute analysis and displacement measurements, *J. Struct. Geol.*, *30*(6), 690–700.
Jin, W., L. Tang, K. Yang, G. Wan, and Z. Lü (2010), Segmentation of the Longmen Mountains thrust belt, western Sichuan foreland basin, SW China, *Tectonophysics*, *485*(1), 107–121.
McGrath, A. G., and I. Davison (1995), Damage zone geometry around fault tips, *J. Struct. Geol.*, *17*(7), 1011–1024.

McLeod, A. E., N. H. Dawers, and J. R. Underhill (2000), The propagation and linkage of normal faults: Insights from the Strathspey-Brent-Statfjord fault array, northern North Sea, *Basin Res.*, *12*, 263–284.
Machette, M. N., S. F. Personius, A. R. Nelson, D. P. Schwartz, and W. R. Lund (1991), The Wasatch fault zone, Utah: Segmentation and history of Holocene earthquakes, *J. Struct. Geol.*, *13*(2), 137–149.
Manighetti, I., P. Tapponnier, V. Courtillot, S. Gruszow, and P. Y. Gillot (1997), Propagation of rifting along the Arabia-Somalia plate boundary: The gulfs of Aden and Tadjoura, *J. Geophys. Res.*, *102*(B2), 2681–2710.
Manighetti, I., P. Tapponnier, P. Y. Gillot, E. Jacques, V. Courtillot, R. Armijo, J. C. Ruegg, and G. King (1998), Propagation of rifting along the Arabia-Somalia plate boundary: Into Afar, *J. Geophys. Res.*, *103*(B3), 4947–4974.
Manighetti, I., G. C. P. King, Y. Gaudemer, C. H. Scholz, and C. Doubre (2001a), Slip accumulation and lateral propagation of active normal faults in Afar, *J. Geophys. Res.*, *106*(B7), 13,667–13,696.
Manighetti, I., P. Tapponnier, V. Courtillot, Y. Gallet, E. Jacques, and P. Y. Gillot (2001b), Strain transfer between disconnected, propagating rifts in Afar, *J. Geophys. Res.*, *106*(B7), 13,613–13,665.
Manighetti, I., G. King, and C. G. Sammis (2004), The role of off-fault damage in the evolution of normal faults, *Earth Planet. Sci. Lett.*, *217*(3), 399–408.
Manighetti, I., M. Campillo, C. Sammis, P. M. Mai, and G. King (2005), Evidence for self-similar, triangular slip distributions on earthquakes: Implications for earthquake and fault mechanics, *J. Geophys. Res.*, *110*, B05302, doi:10.1029/2004JB003174.
Manighetti, I., M. Campillo, S. Bouley, and F. Cotton (2007), Earthquake scaling, fault segmentation, and structural maturity, *Earth Planet. Sci. Lett.*, *253*(3), 429–438.
Manighetti, I., D. Zigone, M. Campillo, and F. Cotton, F. (2009), Self-similarity of the largest-scale segmentation of the faults: Implications for earthquake behavior, *Earth Planet. Sci. Lett.*, *288*(3), 370–381.
Mansfield, C., and J. Cartwright (2001), Fault growth by linkage: Observations and implications from analogue models, *J. Struct. Geol.*, *23*(5), 745–763.
Mansfield, C. S., and J. A. Cartwright (1996), High resolution fault displacement mapping from three-dimensional seismic data: Evidence for dip linkage during fault growth, *J. Struct. Geol.*, *18*(2), 249–263.
Marliyani, G. I., T. K. Rockwell, N. W. Onderdonk, and S. F. McGill (2013), Straightening of the northern San Jacinto fault, California, as seen in the fault-structure evolution of the San Jacinto Valley stepover, *Bull. Seismol. Soc. Am.*, *103*(3), 2047–2061.
Martel, S. J., and C. Shacat, (2006), Mechanics and interpretations of fault slip, *AGU Geophys. Monogr. Ser.*, *170*, 207–215.
Mériaux, A. S., et al. (2005), The Aksay segment of the northern Altyn Tagh fault: Tectonic geomorphology, landscape evolution, and Holocene slip rate, *J. Geophys. Res.*, *110*, B04404, doi:10.1029/2004JB003210.
Mirabella, F., V. Boccali, and M. R. Barchi (2005), Segmentation and interaction of normal faults within the Colfiorito fault system (central Italy), *Geol. Soc. Spec. Publ.*, *243*(1), 25–36.
Nabarro, F. R. N. (1967), *Theory of Crystal Dislocations*, 75 pp., Clarendon, Oxford.
Nicol, A., J. Walsh, K. Berryman, and S. Nodder (2005), Growth of a normal fault by the accumulation of slip over millions of years, *J. Struct. Geol.*, *27*(2), 327–342.
Noda, H., N. Lapusta, and H. Kanamori (2013), Comparison of average stress drop measures for ruptures with heterogeneous stress change and implications for earthquake physics, *Geophys. J. Int.*, *193*(3), 1691–1712, doi:10.1093/gji/ggt074.
Oglesby, D. (2008), Rupture termination and jump on parallel offset faults, *Bull. Seismol. Soc. Am.*, *98*(1), 440–447.
Okubo, P. G., and K. Aki (1987), Fractal geometry in the San Andreas fault system, *J. Geophys. Res.*, *92*(B1), 345–355.
Otsuki, K., and T. Dilov (2005), Evolution of hierarchical self-similar geometry of experimental fault zones: Implications for seismic nucleation and earthquake size, *J. Geophys. Res.*, *110*, B03303, doi:10.1029/2004JB003359.
Pachell, M. A., and J. P. Evans (2002), Growth, linkage, and termination processes of a 10-km-long strike-slip fault in jointed granite: The Gemini fault zone, Sierra Nevada, California, *J. Struct. Geol.*, *24*(12), 1903–1924.
Peacock, D. C. P. (1991), Displacements and segment linkage in strike-slip fault zones, *J. Struct. Geol.*, *13*(9), 1025–1035.
Peacock, D. C. P., and D. J. Sanderson (1991), Displacements, segment linkage and relay ramps in normal fault zones, *J. Struct. Geol.*, *13*(6), 721–733.
Perrin, C., I. Manighetti, Y. Gaudemer, B. Delouis, and M. Campillo (2012), Asymmetry of earthquake slip profiles reveals key properties of the rupture process, Abstract S53A-2477 presented at 2012 Fall Meeting, AGU, San Francisco, Calif.
Pollard, D. D., and P. Segall (1987), Theoretical displacements and stresses near fractures in rock: With applications to faults, joints, veins, dikes, and solution surfaces, *Fract. Mech. Rock*, *277*(349), 277–349.
Power, W. L., and T. E. Tullis (1991), Euclidean and fractal models for the description of rock surface roughness, *J. Geophys. Res.*, *96*(B1), 415–424.
Rabus, B., M. Eineder, A. Roth, and R. Bamler (2003), The shuttle radar topography mission—A new class of digital elevation models acquired by spaceborne radar, *ISPRS J. Photogramm. Remote Sens.*, *57*(4), 241–262.
Renard, F., C. Voisin, D. Marsan, and J. Schmittbuhl (2006), High resolution 3D laser scanner measurements of a strike-slip fault quantify its morphological anisotropy at all scales, *Geophys. Res. Lett.*, *33*, L04305, doi:10.1029/2005GL025038.
Sagy, A., E. E. Brodsky, and G. J. Axen (2007), Evolution of fault-surface roughness with slip, *Geology*, *35*(3), 283–286.
Sammis, C. G., R. M. Nadeau, and L. R. Johnson (1999), How strong is an asperity?, *J. Geophys. Res.*, *104*(B5), 10,609–10,619.
Schlagenhauf, A., I. Manighetti, J. Malavieille, and S. Dominguez (2008), Incremental growth of normal faults: Insights from a laser-equipped analog experiment, *Earth Planet. Sci. Lett.*, *273*(3), 299–311.
Schlagenhauf, A., I. Manighetti, L. Benedetti, Y. Gaudemer, R. Finkel, J. Malavieille, and K. Pou (2011), Earthquake supercycles in Central Italy, inferred from 36Cl exposure dating, *Earth Planet. Sci. Lett.*, *307*(3), 487–500.
Schlische, R. W., S. S. Young, R. V. Ackermann, and A. Gupta (1996), Geometry and scaling relations of a population of very small rift-related normal faults, *Geology*, *24*(8), 683–686.
Scholz, C. H. (1991), Spontaneous formation of space-time and criticality, in *Proceedings of the NATO Advanced Study Institute, Geilo, Norway*, edited by T. Riste and D. Sherrington, pp. 41–56, Kluwer Acad., Dordrecht, Netherlands.
Scholz, C. H. (2002), *The Mechanics of Earthquakes and Faulting*, Cambridge Univ. Press, Cambridge, U. K.
Scholz, C. H., and C. A. Aviles (1986), The fractal geometry of faults and faulting, in *Earthquake Source Mechanics*, edited by S. Das, J. Boatwright, and C. H. Scholz, pp. 147–155, AGU, Washington, D. C., doi:10.1029/GM037p0147.
Scholz, C. H., and J. C. Contreras (1998), Mechanics of continental rift architecture, *Geology*, *26*(11), 967–970.
Scholz, C. H., and T. M. Lawler (2004), Slip tapers at the tips of faults and earthquake ruptures, *Geophys. Res. Lett.*, *31*, L21609, doi:10.1029/2004GL021030.

Schwartz, D. P., and K. J. Coppersmith (1984), Fault behavior and characteristic earthquakes: Examples from the Wasatch and San Andreas fault zones, *J. Geophys. Res.*, *89*(B7), 5681–5698.
Segall, P., and D. D. Pollard (1980), Mechanics of discontinuous faults, *J. Geophys. Res.*, *85*(B8), 4337–4350.
Seno, T. (2003), Fractal asperities, invasion of barriers, and interplate earthquakes, *Earth, Planets and Space*, *55*(11), 649–665.
Shaw, B. E. (2006), Initiation propagation and termination of elastodynamic ruptures associated with segmentation of faults and shaking hazard, *J. Geophys. Res.*, *111*, B08302, doi:10.1029/2005JB004093.
Shaw, B. E., and J. H. Dieterich (2007), Probabilities for jumping fault segment stepovers, *Geophys. Res. Lett.*, *34*, L01307, doi:10.1029/2006GL027980.
Shaw, J. H., A. Plesch, J. F. Dolan, T. L. Pratt, and P. Fiore (2002), Puente Hills blind-thrust system, Los Angeles, California, *Bull. Seismol. Soc. Am.*, *92*(8), 2946–2960.
Sibson, R. H. (1985), Stopping of earthquake ruptures at dilational fault jogs, *Nature*, *316*(6025), 248–251.
Sibson, R. H. (1986), Earthquakes and rock deformation in crustal fault zones, *Annu. Rev. Earth Planet. Sci.*, *14*, 149.
Sibson, R. H. (2003), Thickness of the seismic slip zone, *Bull. Seismol. Soc. Am.*, *93*(3), 1169–1178.
Simoes, M., Y. G. Chen, D. P. Shinde, and A. K. Singhvi (2014), Lateral variations in the long-term slip rate of the Chelungpu fault, Central Taiwan, from the analysis of deformed fluvial terraces, *J. Geophys. Res.*, *119*, 3740–3766, doi:10.1002/2013JB010057.
Soliva, R., and A. Benedicto (2004), A linkage criterion for segmented normal faults, *J. Struct. Geol.*, *26*(12), 2251–2267.
Stirling, M. W., S. G. Wesnousky, and K. Shimazaki (1996), Fault trace complexity, cumulative slip, and the shape of the magnitude-frequency distribution for strike-slip faults: A global survey, *Geophys. J. Int.*, *124*(3), 833–868.
Stein, R. S., P. Briole, J. C. Ruegg, P. Tapponnier, and F. Gasse (1991), Contemporary, Holocene, and Quaternary deformation of the Asal Rift, Djibouti: Implications for the mechanics of slow spreading ridges, *J. Geophys. Res.*, *96*(B13), 21,789–21,806.
Stockwell, R. G., L. Mansinha, and R. P. Lowe (1996), Localization of the complex spectrum: The S transform, *IEEE Trans. Signal Process.*, *44*(4), 998–1001.
Tchalenko, J. S., and M. Berberian (1975), Dasht-e Bayāz fault, Iran: Earthquake and earlier related structures in bed rock, *Geol. Soc. Am. Bull.*, *86*(5), 703–709.
Trudgill, B., and J. Cartwright (1994), Relay-ramp forms and normal-fault linkages, Canyonlands National Park, Utah, *Geol. Soc. Am. Bull.*, *106*(9), 1143–1157.
Van Der Woerd, J., P. Tapponnier, F. J. Ryerson, A. S. Meriaux, B. Meyer, Y. Gaudemer, R. C. Finkel, M. W Caffee, Z. Guoguan, and X. Zhiqin (2002), Uniform postglacial slip-rate along the central 600 km of the Kunlun Fault (Tibet), from 26Al, 10Be, and 14C dating of riser offsets, and climatic origin of the regional morphology, *Geophys. J. Int.*, *148*(3), 356–388.
Walpersdorf, A., et al. (2014), Present-day kinematics and fault slip rates in eastern Iran, derived from 11 years of GPS data, *J. Geophys. Res.*, *119*, 1359–1383, doi:10.1002/2013JB010620.
Walsh, J. J., and J. Watterson (1988), Analysis of the relationship between displacements and dimensions of faults, *J. Struct. Geol.*, *10*(3), 239–247.
Walsh, J. J., and J. Watterson (1990), New methods of fault projection for coalmine planning, *Proc. Yorkshire Geol. Soc.*, *48*, 209–219.
Walsh, J. J., and J. Watterson (1991), Geometric and kinematic coherence and scale effects in normal fault systems, *Geol. Soc. Spec. Publ.*, *56*(1), 193–203.
Walsh, J. J., W. R. Bailey, C. Childs, A. Nicol, and C. G. Bonson (2003), Formation of segmented normal faults: A 3-D perspective, *J. Struct. Geol.*, *25*(8), 1251–1262.
Wang, Y., B. Zhang, J. Hou, and X. Xu (2014), Structure and tectonic geomorphology of the Qujiang fault at the intersection of the Ailao Shan-Red River fault and the Xianshuihe-Xiaojiang fault system, China, *Tectonophysics*, *634*, 156–170.
Werner, M. (2001), Shuttle radar topography mission (SRTM) mission overview, *Frequenz*, *55*(3–4), 75–79.
Wesnousky, S. G. (1988), Seismological and structural evolution of strike-slip faults, *Nature*, *335*, 340–343, doi:10.1038/335340a0.
Wesnousky, S. G. (2006), Predicting the endpoints of earthquake ruptures, *Nature*, *444*(7117), 358–360.
Wesnousky, S. G. (2008), Displacement and geometrical characteristics of earthquake surface ruptures: Issues and implications for seismic-hazard analysis and the process of earthquake rupture, *Bull. Seismol. Soc. Am.*, *98*(4), 1609–1632.
Wesnousky, S. G., and G. P. Biasi (2011), The length to which an earthquake will go to rupture, *Bull. Seismol. Soc. Am.*, *101*(4), 1948–1950.
Willemse, E. J. (1997), Segmented normal faults: Correspondence between three-dimensional mechanical models and field data, *J. Geophys. Res.*, *102*(B1), 675–692.
Wu, D., and R. L. Bruhn (1994), Geometry and kinematics of active normal faults, South Oquirrh Mountains, Utah: Implication for fault growth, *J. Struct. Geol.*, *16*(8), 1061–1075.
Young, M. J., R. L. Gawthorpe, and S. Hardy (2001), Growth and linkage of a segmented normal fault zone; the Late Jurassic Murchison-Statfjord North Fault, northern North Sea, *J. Struct. Geol.*, *23*(12), 1933–1952.
Zhang, P., D. B. Slemmons, and F. Mao (1991), Geometric pattern, rupture termination and fault segmentation of the Dixie Valley—Pleasant Valley active normal fault system, Nevada, USA, *J. Struct. Geol.*, *13*(2), 165–176.
Zhang, P., F. Mao, and D. B. Slemmons (1999), Rupture terminations and size of segment boundaries from historical earthquake ruptures in the Basin and Range Province, *Tectonophysics*, *308*(1), 37–52.